

Investigation into a Homogenous Rock Slope Response Under Wide Frequency Seismic Loads Using a Large-Scale Shaking Table

Jianxian He

Southwest Jiaotong University

Zhifa Zhan

China Renewable Energy Engineering Institute

Shengwen Qi (✉ qishengwen@mail.igcas.ac.cn)

Institute of Geology and Geophysics Chinese Academy of Sciences <https://orcid.org/0000-0002-0967-7582>

Chunlei Li

IWHR: China Institute of Water Resources and Hydropower Research

Bowen Zheng

Institute of Geology and Geophysics Chinese Academy of Sciences

Guoxiang Yang

China University of Geosciences

Songfeng Guo

Institute of Geology and Geophysics Chinese Academy of Sciences

Xiaolin Huang

Institute of Geology and Geophysics Chinese Academy of Sciences

Yu Zou

Institute of Geology and Geophysics Chinese Academy of Sciences

Ning Liang

Institute of Geology and Geophysics Chinese Academy of Sciences

Research Article

Keywords: Seismic response of the slope, Wide frequency effect, topography effect, Shaking table test, Resonance effect

Posted Date: August 20th, 2021

DOI: <https://doi.org/10.21203/rs.3.rs-770591/v1>

License: © ⓘ This work is licensed under a Creative Commons Attribution 4.0 International License.

[Read Full License](#)

19 **Declarations**

20

21 **Funding**

22 This work was financially supported by the National Natural Science Foundation of China
23 under grants of 41825018, 41672307 and 41790442, and the Second Tibetan Plateau Scientific
24 Expedition and Research Program (STEP) under grant of No. 2019QZKK0904.

25

26 **Conflicts of interest**

27 The authors declare that they have no conflict of interest.

28

29 **Availability of data and material**

30

31 All data and material have been enclosed in the manuscript.

32

33 **Code availability**

34

35 Not applicable.

36

37 **Authors' contributions**

38

39 Jianxian He processes data and drafts this manuscript. Zhifa Zhan designs the physical model
40 and carries out the experiment. Chunlei Li carries out the experiment. Bowen Zheng,
41 Guoxiang Yang, Songfeng Guo, Xiaolin Huang, Yu Zou and Ning Liang provide suggestions
42 and help to revise the manuscript. Shengwen Qi conceives the idea and experimental scheme,
43 provides the financial support and revises the manuscript.

44

45 **Authors' E-mail addresses:**

46 1) Jianxian He, E-mail: hejianxian91@swjtu.edu.cn;

47 2) Zhifa Zhan, E-mail: zhanzhifa100@126.com;

48 3) Shengwen Qi, E-mail: qishengwen@mail.iggcas.ac.cn;

49 4) Chunlei Li, E-mail: 251225788@qq.com;

50 5) Bowen Zheng, E-mail: zhengbowen@mail.iggcas.ac.cn;

- 51 6) Guoxiang Yang, E-mail: 570966297@qq.com;
- 52 7) Songfeng Guo, E-mail: guosongfeng@mail.iggcas.ac.cn;
- 53 8) Xiaolin Huang, E-mail: huangxiaolin@mail.iggcas.ac.cn;
- 54 9) Yu Zou, E-mail: zouyu@mail.iggcas.ac.cn;
- 55 10) Ning Liang, E-mail: liangning@mail.iggcas.ac.cn.
- 56

57 **Abstract:** The main objective of this study was to investigate the effect of input earthquake
58 characteristics on the seismic response of a homogenous step-like rock slope. A sequence of
59 shaking table tests was performed in a large-scale physical model with a size of 3.50 m, 0.68
60 m and 1.20 m in length, width and height, respectively. Results showed that the absolute
61 peak ground acceleration motion amplification factor in horizontal direction (AAF-X)
62 of upper part of the slope was amplified comparison with that at the slope toe while the
63 absolute peak ground acceleration motion amplification factor (AAF-Z) acquired
64 maximum value at the lower position of the slope. With the increasing of the excitation
65 frequencies, the AAF-X around the slope crest increased firstly and then decreased,
66 while the AAF-Z increased continuously. Seismic response of the slope showed
67 strongest amplification when the normalized height of the slope H/λ (ratio of slope
68 height to wavelength) was around 0.2 and AAF-X exhibited a decrease trend when H/λ
69 was larger than 0.2. The AAF showed nonlinear tendency with the increases of the input
70 amplitudes, especially near the shoulder of the slope. This phenomenon can be revealed
71 by the relationship between the calculated resonance frequency or damping ratio of the
72 slope and the amplitude of the input motion. The excitation amplitude has a “double-
73 effect” on the seismic response of a step-like homogeneous rock slope. That is on the
74 one hand, the larger the excitation amplitude, the stronger the acceleration intensity, the
75 greater deterioration of rock slope structure or material and the larger damping ratio of
76 the slope; on the other hand, more energy will be dissipated due to plastic deformation
77 or particle friction of high damping ratio and weaker slope structure. These results could
78 attribute to reveal the dynamic instability mechanism of the homogeneous slope.

79 **Keywords:** Seismic response of the slope; Wide frequency effect; topography effect;
80 Shaking table test; Resonance effect

81 **1 Introduction**

82 In recent decades, plenty of landslides were often triggered by strong earthquakes,
83 such as 1999 M_L 7.3 earthquake occurred in Chi-Chi (Khazai and Sitar, 2004; Sepulveda
84 et al., 2005), 2005 M_W 7.6 Kashmir earthquake in Pakistan (Owen et al., 2008), 2008
85 M_W 7.9 earthquake occurred in Sichuan (Qi et al., 2010; Yin et al., 2009), and 2010 M_W
86 7.0 earthquake in Haiti (Hough et al., 2010). Some catastrophic co-seismic landslides
87 generally induced lots of casualties and loss of properties. Especially for 2008
88 Wenchuan earthquake with M_W 7.9, it statically brought about over 15,000 landslides
89 and caused 20,000 deaths directly (Qi et al., 2010; Yin et al., 2009). A co-seismic
90 landslide is the dynamic progressive destruction of the slope material under seismic
91 stress waves. The dynamic response of a rock slope under earthquake is the basic issue
92 of understanding the instability mechanism of this kind geo-hazard and taking measures
93 in prevention and mitigation. Some previous studies showed the seismic response of a
94 slope significantly depended on the loading frequency and amplitude of the earthquake
95 (Lin and Wang, 2006; Liu et al., 2013; Srilatha et al., 2013). Field observations,
96 numerical simulations and physical modelling tests are often applied in the study of this
97 subject.

98 Field monitoring data revealed that peak ground motion acceleration (PGA) at
99 upper part or shoulder of a slope or ridge was amplified compared to that at the toe or
100 base. Solid evidences for this phenomenon were monitoring data on the Kagel mountain

101 in California (Davis and West, 1973), Chusal valley in Tien Shan Mountain (Tucker et
102 al., 1984), Robinwood ridge in California (Hartzell et al., 1994), mountains in
103 Caramanico area of central Italy (Del Gaudio and Wasowski, 2007), Weigan hill,
104 Mountain Shizi in Qingchuan county Sichuan province (Luo et al., 2014) and
105 Lengzhuguan slope (He et al., 2020; Wang et al., 2017). Nevertheless, because of strong
106 randomness of the seismic load, limited monitoring data and the complicated slope
107 structure, it is almost impossible to quantitatively characterize seismic response of the
108 slope and establish theoretical model via monitoring data. Meanwhile, numerical
109 simulation results also exhibited that PGA increased along the slope surface with
110 elevation increasing, especially at the slope crest (Geli et al., 1988; Ashford et al., 1997;
111 Qi et al., 2003; Bouckovalas and Papadimitriou, 2005; Qi, 2006; Hailemikael et al.,
112 2016). However, due to complicated dynamic behavior of geo-material and boundary
113 effect, the mechanical behavior and progressive failure under earthquake still cannot be
114 perfectly simulated using the existed numerical simulation methods. The physical
115 model test, like shaking table test, is a feasible and popular way to uncover the seismic
116 response characteristics of a slope. Hence, the seismic response characteristics of a
117 model is quantitatively evaluated in detail. It has some advantages such as the control
118 on the frequency, amplitude and duration of the loads. Furthermore, discontinuity
119 properties of the slope can be preliminarily designed and its progressive failure under
120 seismic loading can be fully observed by combination of the optical technique such as
121 the high-speed camera. Wartman et al. (2005) found that the generated permanent
122 deformations were varied along the different location of the slope model under strong

123 seismic loadings. Meanwhile, nonlinear seismic response was observed when the
124 amplitude of the dynamic load was over 0.4 g, and the slope surface exhibited the
125 strongest seismic response through physical models (Lin and Wang, 2006; Liu et al.,
126 2013). Liu et al. (2013) also found that PGAs in the horizontal direction showed an
127 increasing trend at the surface of the slope and abruptly amplified at the crest derived
128 from physical modelling under Wenchuan earthquake. Shi et al. (2015a) and Shi et al.
129 (2015b) found that the accelerations were generally amplified on the surface of
130 landslide dams and content of fine particles could effect the failure mode of the dam.
131 Some researchers also noted that discontinuities in rock masses affected the seismic
132 response of the slope and control failure mechanism under earthquakes (Fan et al., 2016;
133 Song et al., 2018a; Song et al., 2018b; Yang et al., 2018b; He et al., 2021). Physical
134 modeling results was also applied to verify the analytical stability solution for rock
135 slope under earthquake (Guo et al., 2017). However, the frequency of the loads involved
136 in these studies only covered a limited range which were often smaller than intrinsic
137 vibration frequency of the slope. Moreover, the resonance frequencies of the physical
138 models were high and also progressively changed under seismic loads. The seismic
139 loads with wide frequency should thus be considered to capture the practical case.
140 Meanwhile, the range of the frequency which significantly influences the seismic
141 response of the model should be quantitatively determined derived from the natural
142 frequency of the slope. Another crucial point should also be taken into account, that is,
143 the resonance frequency of a slope is not a constant, and it varies with the progressive
144 failure of the slope as a result of damage occurred during earthquake.

145 From the reviews on previous studies, the motivation of this paper is to deeply
146 reveal the dynamic response of the step-like homogeneous rock slope under earthquake
147 with a wide frequency and amplitude. This paper is organized in the following way:
148 Section 1 reviews the previous studies related to the seismic response of the step-like
149 homogeneous slope and analyzes the limitations in these studies. Section 2 introduces
150 the method used including the derivation of the similitude equations on the physical
151 modeling, the preparation of the physical model and data processing technique. Section
152 3 analyses the data gathered. Section 4 analyses the results and focuses on discussion
153 on the results. Section 5 presents the findings and conclusions of the research.

154 **2 Methodology**

155 Shaking table test on the physical slope model in the laboratory is to simulate the
156 seismic response of the prototype slope in the laboratory. That is, the prototype slope is
157 substituted with a physical model on the shaking table and the dimension, physical
158 properties and seismic load obey the law of similitude. This physical simulation is a
159 scaling-down process in which the seismic response characteristics and failure behavior
160 can be finely investigated considering different pre-design conditions. In this study, the
161 effect of excitation earthquake characteristics including frequency and amplitude on on
162 the seismic response of the slope is mainly investigated and progressive change law of
163 resonance frequency of the slope is also considered with the increasing of the amplitude.
164 A large-scale homogenous rock slope model is adopted for simplicity and restricting
165 the number of factors such as rock mass structure. In this section, the derivation of
166 similarity equations is introduced firstly, then the preparation of the physical model is

167 described in details, and the test procedure and data processing technique are finally
168 presented.

169 **2.1 Derivation of similitude equations**

170 The similitude relations are obtained based on similarity three theorems (Brand,
171 1957) which have been widely applied in the physical simulation on mechanical
172 behavior of soils under static or earthquake loading rate (Iai, 1989; Lin and Wang, 2006;
173 Liu et al., 2013; Fan et al., 2016). In the study, sixteen parameters (influence factors)
174 are considered. Meanwhile, three dimensional parameters are selected as fundamental
175 variables, i.e., geometric dimension l , density of the material ρ and acceleration a .
176 Hence, following equation should be satisfied (Fan et al., 2016):

$$177 \quad f(l, \rho, a, c, \varphi, E, \mu, \sigma_c, \sigma_t, \sigma, \varepsilon, u, v, g, \omega, t) = 0 \quad (1)$$

178 where, l is the geometric dimension, ρ is density of the rock mass, a is the acceleration,
179 c is the cohesion of the rock mass, φ is the friction angle of the material, E is elasticity
180 modulus, μ is Poisson's ratio, σ_c is the uniaxial compressive strength, σ_t is tensile
181 strength, σ represents the stress of the model, ε is the strain caused by stress, u is the
182 displacement, v is the velocity, g gravitational acceleration, ω angular frequency, and t
183 the time (He, et al., 2021).

184 Through dimensional analysis, the dimensions of the considered parameters in Eq. (1)
185 is the function of three fundamental parameters $[L]$ (geometric dimension), $[T]$ time and
186 $[M]$ mass. (He, et al., 2021). Table 1 lists the dimension factor of the variables adopted
187 in shaking table test.

188 **Table 1 The dimension factor of the variables adopted physical model test**

189 The following equation can be obtained by combining each term (Cao et al., 2020):

190

$$M^0 L^0 T^0 = L^{a_1} \cdot (ML^{-3})^{a_2} \cdot (LT^{-2})^{a_3} \cdot (ML^{-1}T^{-2})^{a_4} \cdot (1)^{a_5} \cdot (ML^{-1}T^{-2})^{a_6} \cdot (1)^{a_7} \cdot (ML^{-1}T^{-2})^{a_8} \cdot (ML^{-1}T^{-2})^{a_9} \cdot (ML^{-1}T^{-2})^{a_{10}} \cdot (1)^{a_{11}} \cdot (L)^{a_{12}} \cdot (LT^{-1})^{a_{13}} \cdot (LT^{-2})^{a_{14}} \cdot (T^{-1})^{a_{15}} \cdot (T)^{a_{16}} \quad (2)$$

191 According to dimensional consistency and Eq. (2), Eq. (3) can be reached:

192

$$\begin{cases} a_2 + a_4 + a_6 + a_8 + a_9 + a_{10} = 0 \\ a_1 - 3a_2 + a_3 - a_4 - a_6 - a_8 - a_9 - a_{10} + a_{12} + a_{13} + a_{14} = 0 \\ -2a_3 - 2a_4 - 2a_6 - 2a_8 - 2a_9 - 2a_{10} - a_{13} - 2a_{14} - a_{15} + a_{16} = 0 \end{cases} \quad (3)$$

193 Meanwhile, based on the $[L]$, $[T]$ and $[M]$ three fundamental dimensions, we can

194 write the similarity criterion functions of Eq. (1) as follows:

195

$$F(\pi_1, \pi_2, \pi_3, \dots, \pi_{13}) = 0 \quad (4)$$

196 where, π_i represents similarity criterion.

197 According to Eq. (3), similarity criterion π_i can be obtained in the following

198 equation:

199

$$\pi_i = [l]^{a_1} \cdot [\rho]^{a_2} \cdot [a]^{a_3} \cdot [c]^{a_4} \cdot [\varphi]^{a_5} \cdot [E]^{a_6} \cdot [\mu]^{a_7} \cdot [\sigma_c]^{a_8} \cdot [\sigma_t]^{a_9} \cdot [\sigma]^{a_{10}} \cdot [\varepsilon]^{a_{11}} \cdot [u]^{a_{12}} \cdot [v]^{a_{13}} \cdot [g]^{a_{14}} \cdot [\omega]^{a_{15}} \cdot [t]^{a_{16}} \quad (5)$$

200 Finally, thirteen similarity criterion π_i are obtained through matrix method and the

201 similarity criterion is shown in Table 2.

202 **Table 2 The similarity criterion in the shaking table test**

203 As mentioned above, l , ρ and a are set as fundamental quantities or controlling

204 parameters with scaling factor $C_l=100$, $C_\rho=1$ and $C_a=1$, respectively. Finally, scaling

205 factor of each considered variable can be calculated using the similarity criterion in

206 Table 2 and the calculated factors are listed in Table 3.

207 **Table 3 The similarity ratios of considered parameters**

208 **2.2 Details of the shaking table**

209 Fig. 1 shows the shaking table apparatus which is housed in Earthquake

210 Engineering Research Center, China Institute of Water Resources and Hydropower
211 Research (IWHR) (He et al., 2021). This table has six degrees of freedom and it can
212 translate and rotate in three directions. The length and width of shaking table are both
213 5 m. The excitation frequency of the shaking table facility is between 0.1 Hz and 120
214 Hz. The load capacity and maximum overturn moment are 20,000 kg and 343 kN·m,
215 respectively. The acceleration in horizontal reaches 1.0 g and the acceleration in vertical
216 can reach 0.7 g, under the full loading of the shaking table. Accordingly, this shaking
217 table can completely fulfill our research requirement to study the seismic response of a
218 step-like homogeneous rock slope under wide frequency and amplitude excitation.

219 **Fig. 1. Layout of the shaking table at IWHR**

220 **2.3 Model preparation**

221 In this section, the equivalent materials should be determined to establish the
222 physical model. Several types of equivalent materials such as sand and soils were
223 reported to mold the physical model in previous shaking table tests (Wartman et al.,
224 2005; Wang and Lin, 2011; Srilatha et al., 2013). In this study, the similar material is
225 based on the results of Zhan et al. (2019). To achieve more reliable results, the physical
226 model is strictly fulfilled the similarity ratio derived in this paper and can reflect the
227 natural slope furthest.

228 By trial and error, the equivalent materials have been reached by mixing iron ore
229 powder, barites powder, quartz sand, gypsum powder, cement and water (Zhan et al.,
230 2019). The first three materials are used as aggregate materials. Gypsum powder and
231 cement are adopted as regulator materials. The water is applied as glue. Then

232 orthogonal tests are applied to determine the effect of each material proportion on the
233 mechanical properties (such as uniaxial compressive strength) of the equivalent
234 materials via uniaxial compression tests, tensile tests and direct shear tests. After many
235 trials, the best weight proportion of iron ore powder, barites powder, quartz sand,
236 gypsum powder, cement and water are 7.5:38.6:38.6:4.1:1.7:9.6, to well simulate the
237 rock mass. The parameters of the similarity material from various tests are listed in
238 Table 4, updated after Zhan et al. (2019).

239 **Table 4 Parameters of the similarity material**

240 The homogenous slope model was constructed in a rigid steel box and the length,
241 width and height of the box are 3.57 m, 0.7 m, 1.25 m, respectively. Meanwhile, the
242 slope was smaller than the box with a size of 3.5 m × 0.68 m × 1.20 m (length × width
243 × height).

244 A thickness of 30 cm equivalent material was firstly paved at the bottom of the
245 physical model base. Rigid steel boxes were widely used as slope container in previous
246 shaking table tests (Wartman et al., 2005; Lin and Wang, 2006; Liu et al., 2013; He et
247 al., 2021). Nevertheless, influences of the rigid boundary may interfere experimental
248 result. To overcome this problem, it was suggested that an absorber composed of
249 polystyrene material can be used to minimize this influence, allowed for a “reasonably
250 correct” (Wartman et al., 2005; Lin and Wang, 2006). In this study, damping liquid
251 composed of hydrocarbon polymers was placed on the north and south sides between
252 the slope and box to eliminate the boundary effect (He et al., 2021). By comparing
253 monitoring data between accelerometer near boundary and inside of the slope in the

254 following section, it indicated that the error can be restricted in a reasonable range.

255 Equivalent materials were produced in a stirrer by mixing basic materials strictly
256 according to the weight proportion. Then equivalent materials were put into the model
257 container and compacted to the design mass density with a thickness of 5 cm.
258 Meanwhile, templates were used to ensure slope angle at the designed 45° during the
259 building-up procedure. Finally, it took about two weeks to construct the physical model
260 and one week to naturally dry. Fig. 2 shows the final homogenous slope model.

261 **Fig. 2. The front view of the physical model before test**

262 As shown in Fig. 3, 21 three-component accelerometers marked A02, A03, ...,
263 A22, are installed in or at the surface of the slope in North-South direction of the slope
264 model. The measurement range of accelerometer is between -0.5 g to +0.5 g under
265 working frequency 0.1-1000 Hz. Accelerometer sensor A01 is installed on the table to
266 monitor the excitation acceleration.

267 **Fig. 3. Schematic design of the physical model (unit: mm)**

268 **2.4 Input motions**

269 In current study, the seismic response of the step-like homogeneous slope under
270 harmonic shear excitations in X-direction was mainly considered. The frequency of the
271 harmonic excitations was set to 15 Hz to 75 Hz with an interval of 15 Hz. Meanwhile,
272 the input amplitudes of the ground motions were set to 0.1 g to 0.5 g with an interval
273 of 0.1 g. Meanwhile, the seismic duration was set to 10 s. Before and after each test, a
274 white noise (WN) scanning was excited at the base to monitor the intrinsic frequency
275 and damping ratio of the slope. The details of the input motions were listed in Table 5.

Table 5 The excitation scheme

276

277 2.5 Data processing method

278 Firstly, recorded accelerations were processed by baseline correction using
279 moving average method and Butterworth bandpass filtering in software MATLAB 9.0.
280 Then, absolute values of the peak accelerations in horizontal direction and vertical
281 direction were determined in time domain. Furthermore, based on recorded signals
282 under the WN excitation, transfer functions at different location of the model slope
283 comparing with that at shaking table base can be determined using the following
284 function *tfestimate* built in MATLAB.

285

$$T(\omega, h_m) = \frac{G_{XY}(\omega, \omega_m)}{G_{XX}(\omega, \omega)} \quad (6)$$

286 where, $T(\omega, h_m)$ denotes the transform function of monitoring point m (h_m is the
287 elevation of point m), $G_{XY}(\omega, \omega_m)$ the acceleration cross power spectrum between point
288 m and shaking table base, and $G_{XX}(\omega, \omega)$ the auto power spectrum of shaking table base.
289 Then, resonance frequency of the slope model can be determined through the transform
290 function curve. Meanwhile, damping ratio can be calculated through half-power
291 bandwidth method suggested by Jiang et al. (2010):

292

$$\lambda = \frac{\omega_2 - \omega_1}{2\omega_0} \text{ and } \omega_1 < \omega_2 \quad (7)$$

293 where, ω_0 denotes the corresponding frequency of peak, ω_1 and ω_2 the corresponding
294 frequency where the value is equal to half peak in bilateral sides of the transform
295 function curve.

296 3 Results

297 In the following text, the frequency and amplitude of the input excitation are

298 shortened as frequency and amplitude for simplicity. For the convenience of description,
299 the definition of acceleration amplification factors (AAF) is the ratio of PGAs
300 monitored in the slope to that at the slope toe A22 and AAF-X and AAF-Z represent the
301 AAF in horizontal direction and vertical direction (Yang et al., 2018b; He et al., 2021),
302 respectively. Meanwhile, we also define a dimensionless parameter, normalized height
303 χ which is the ratio of the Z coordinate of accelerometer h (the coordinate origin is set
304 at the slope toe A22) the slope height H (H , relative height from the slope crest to the
305 toe).

306 **3.1 Influence of frequency**

307 In this section, the frequency of the excitation motions varied while the PGA of
308 input motion was fixed to investigate seismic response of the slope dependency on
309 frequency. Previous studies revealed that slope would appear nonlinear seismic
310 response when input amplitude was larger than 0.3 g (Lin and Wang, 2006; Liu et al.,
311 2013). Hence, input amplitude of 0.1 g was analyzed in this section.

312 **3.1.1 AAF-X analysis result**

313 Fig. 4 shows pseudo-color contour maps based on AAF-X data considered
314 different frequency of the shear load with same amplitude and duration. It shows that
315 the AAF-X increases with χ and it has a significant amplification at the slope crest slope
316 when the input frequency is smaller than 60 Hz. Nevertheless, when the frequency is
317 60 Hz and 75 Hz, the AAF-X decreases firstly and then increases with the increasing
318 of χ . Results show that the AAF-X of the slope crest attain maximum value when the
319 load frequency is 45 Hz.

320 **Fig. 4. AAF-X distribution along slope section under the excitation amplitude of**
321 **0.1g with different frequency: (a) – (e) are from 15 Hz to 75 Hz with an interval**
322 **of 15 Hz**

323 Furthermore, three different sections, i.e., along the slope surface (A22, A02, A03,
324 A04), along the horizontal direction H1 (A22, A10, A09, A08, A07, A06) and along the
325 vertical direction V1 (A08, A12, A15, A04) are chosen to understand the AAF-X
326 change law in detail, as shown in Fig. 3.

327 Fig. 5(a) exhibits the change law of the AAF-X along the surface. It clearly shows
328 that the AAF-X increases with χ increasing from slope toe to crest and gets maximum
329 value at the slope crest, when the input frequency is 15 Hz, 30 Hz and 45 Hz. The AAF-
330 X of each point also increases with frequency increasing and it has the largest value at
331 crest when the frequency is equal to 45 Hz. However, when the frequency is equal to
332 60 and 75 Hz, the AAF-X decreases firstly and then it increases after passing a valley
333 (χ is around 1/3) with the increase of χ . It can be also observed that the AAF-X at crest
334 is less than 1.0 when the frequency is 75 Hz, while the value is 1.54 when the frequency
335 is 60 Hz, which is much larger than that when the frequency is 15 Hz and 30 Hz but
336 smaller than that when the frequency is 45 Hz.

337 Fig. 5(b) shows the AAF-X along the vertical direction V1. It indicates that the
338 AAF-X of the A08 at bottom is around 1.0 when the frequency is smaller than 60 Hz,
339 while the value is smaller than 0.5 when the frequency is 60 and 75 Hz. It also reveals
340 that the AAF-X increases when the χ increase and reaches largest value at the crest.
341 Furthermore, the increase rate of the AAF-X also shows an increasing tendency along
342 the V1 when the input frequency is 15 Hz, 30 Hz and 45 Hz.

343 Fig. 5(c) exhibits the change law of AAF-X along section H1. It clearly shows that
344 the AAF-X increases slightly from the inner part slope to the slope surface at the
345 beginning, then it only varies slightly and keeps a constant around 1.0 when the
346 frequency is 15 Hz and 30 Hz. The AAF-X basically increases nonlinearly outward to
347 the surface when the horizontal distance is larger than 30 cm while it decreases at the
348 slope surface when the frequency is 45 Hz. It can be found that the AAF-X varies
349 slightly from the point A06 to the point A10 while it increases dramatically at the slope
350 surface when the frequency is 60 Hz and 75 Hz.

351 **Fig. 5. The AAF-X change law of different sections (a) slope surface, (b) V1 and**
352 **(c) H1 under the excitation amplitude of 0.1g**

353 3.1.2 AAF-Z analysis result

354 Fig. 6 exhibits pseudo-color contour maps of the AAF-Z when considering
355 different frequency. It shows that the AAF-Z firstly increases with increasing of χ , then
356 it decreases when χ is over 1/3. Meanwhile, it indicates that the AAF-Z can exceed 3.0
357 when the frequency is 75 Hz while others are less than 2.55 when χ is around 1/3.
358 Moreover, three different sections aforementioned are also used to reveal the variation
359 characteristics of AAF-Z in detail.

360 **Fig. 6. AAF-Z distribution along the slope section under the excitation amplitude**
361 **of 0.1g with different frequency: (a) – (e) are from 15 Hz to 75 Hz with an interval**
362 **of 15 Hz**

363 Fig. 7(a) indicates that the AAF-Z also increase with χ increasing when the χ is
364 smaller than 1/3, and then it decreases with the increase of χ and it finally achieves the
365 minimum at the crest of the slope. It can be also seen that the AAF-Z has the maximum

366 value when the frequency is 75 Hz for the same χ . When the frequency is 30 Hz, the
367 AAF-Z at the crest is smaller than 1.0 while others are over 1.0.

368 Fig. 7(b) shows the AAF-Z along the vertical direction V1. Overall, the AAF-Z
369 exhibits a lying “Z-shaped” change law along the section V1 when the frequency is 45
370 Hz, 60 Hz and 75 Hz. Nevertheless, the AAF-Z increases along the section V1 when
371 frequency is 30 Hz and it decreases firstly and then increases when frequency is 15 Hz.
372 It also can be seen that the AAF-Z of point A08 at the bottom approximates 1.0 when
373 the frequency is 15 Hz, 45 Hz and 60 Hz, while corresponding values fluctuate around
374 1.0 when the frequency is 30 Hz and 75 Hz.

375 Fig. 7(c) exhibits the AAF-Z along the horizontal direction H1. It shows that the
376 AAF-Z almost increases with the decrease of the horizontal depth from accelerometer
377 A06 to accelerometer A22, while it has a sharp decrease near the surface of the slope.
378 Meanwhile, the larger excitation frequency, the wider decrease range. It can be also
379 seen that the curve for the frequency of 15 Hz has relatively slight variation trend
380 comparing with other curves.

381 **Fig. 7. The AAF-Z along the (a) slope surface, (b) H1 and (c) V1 under the**
382 **excitation amplitude of 0.1g**

383 **3.2 Influence of amplitude**

384 **3.2.1 AAF-X analysis result**

385 Fig. 8 shows the contour maps of AAF-X in the slope when the amplitude varies
386 but the frequency keeps a constant of 15 Hz. It indicates that the AAF-X increases with
387 the increasing of the excitation amplitude when the amplitude is between 0.1 g to 0.3 g,

388 especially at the crest of the slope. Nevertheless, the AAF-X shows a decreasing trend
389 when the amplitude increases from 0.3 g to 0.5 g. Three sections aforementioned along
390 surface, H1 and V1, are also analyzed in this section to study seismic response
391 characteristics.

392 **Fig. 8. AAF-X distribution along the slope section under the excitation frequency**
393 **15 Hz with different amplitude: (a) – (e) are from 0.1 g 0.5 g with an interval of**
394 **0.1 g**

395 Fig. 9(a) shows the variation characteristic of the AAF-X along surface. It
396 indicates that the AAF-X increases when χ increasing as the input amplitude is between
397 0.1 g and 0.4 g. Nevertheless, the AAF-X shows a decreasing trend firstly and then
398 increases as the amplitude reaches 0.5 g. Meanwhile, the AAF-X at the slope crest is
399 also smaller than that at the slope toe. It also indicates that AAF-X at the same location
400 increases firstly and then decreases with the increasing of the excitation amplitude and
401 the turning amplitude is 0.4 g. Furthermore, the variation of the AAF-X for the
402 amplitude of 0.5 g is different from others.

403 Fig. 9(b) displays the AAF-X along the vertical direction V1. It shows the same
404 change law as that along the slope surface with χ increasing. Meanwhile, the AAF-X at
405 the same χ increases with the increment of the excitation amplitude, when the excitation
406 amplitude varies from 0.1 g to 0.4 g. Nevertheless, when the amplitude reaches 0.5g,
407 the AAF-X at the bottom (A08) is smaller than 1.0, and shows a decreasing tendency.

408 Fig. 9(c) shows the AAF-X along H1 section. It shows that the AAF-X has a big
409 increase at the beginning, then it undergoes a slightly increase and then decreases from
410 the inner monitoring accelerometer to surface monitoring point when the excitation

411 amplitude varies from 0.1 g to 0.4 g. However, the AAF-X increases with decreasing
412 of horizontal distance from inner position to the surface of the slope and all of the values
413 are smaller than 1.0.

414 **Fig. 9. The AAF-X change law of different sections (a) slope surface, (b) H1 and**
415 **(c) V1 under the excitation frequency 15 Hz**

416 3.2.2 AAF-Z analysis result

417 Fig. 10 shows the AAF-Z pseudo-color contour maps when amplitudes varies but
418 the frequency keeps a constant of 15 Hz. It indicates that the AAF-Z is amplified at the
419 lower part of the slope (approximately at the χ of 1/3). Besides, the AAF-Z behaves
420 obvious amplification when the amplitude is 0.4 g.

421 **Fig. 10. AAF-X distribution along the slope section under the excitation**
422 **frequency 15 Hz with different amplitude: (a) – (e) are from 0.1 g to 0.5 g with an**
423 **interval of 0.1 g**

424 Fig. 11(a) shows that the variation characteristic of the AAF-Z along the slope
425 surface. It indicates that the AAF-Z increases dramatically firstly and then decreases
426 with increasing of χ . Meanwhile, the AAF-Z reaches largest value (2.27) at the location
427 of χ equal to 1/3 when the amplitude is 0.4 g. Nevertheless, the AAF-Z shows the
428 weakest response as the amplitude reaches 0.5 g. Fig. 11(b) exhibits the AAF-Z along
429 the vertical section V1. It can be seen that AAF-Z shows decreasing trend firstly and
430 then exhibits increasing trend with the increasing of the χ and it reaches the maximum
431 at the crest. Nevertheless, the AAF-Z with the amplitude 0.5 g is smaller than the cases
432 of other input amplitudes. Fig. 11(c) shows the AAF-Z along the horizontal direction
433 H1. The AAF-Z shows a trend of fluctuating increase to its peak value and then has a

434 slight decrease to 1.0 when the amplitude is 0.1g, 0.3g or 0.4g. Nevertheless, the AAF-
435 Z shows a trend of fluctuating decrease once the amplitude is 0.2g and then has a slight
436 increase to 1.0, and the AAF-Z reaches the maximum at the slope surface once the
437 amplitude is 0.5 g. It should also be noted that the AAF-Z has a much less value at the
438 same monitor point once the amplitude is 0.5g.

439 **Fig. 11. The AAF-Z change law of different sections (a) slope surface, (b) H1 and**
440 **(c) V1 under the excitation frequency 15 Hz**

441 **4 Discussion**

442 In shaking table test, the law of similitude cannot be perfectly fulfilled and the
443 rigid boundary might affect the wave transmission in the study. However, Lin and Wang
444 (2006) suggested that dynamic failure surface of the slope would not or slightly affect
445 by the boundary if the distance from the slope crest to box boundary behind the slope
446 crest was longer than or equal to twice horizontal slope length. Our model meets the
447 criterion suggested by Lin and Wang (2006). Furthermore, the absolute difference
448 percentage (Δa) is defined as the difference between the AAF-X of monitoring point
449 near the boundary (A19) and that in the middle part of the slope (A18) divided by that
450 value of accelerometer A18. Fig. 12 shows Δa under different input motion excitations.
451 It exhibits that average Δa is below 20%. Therefore, “reasonably correct” test data
452 obtained in this study can reveal the dynamic response law of the step-like homogenous
453 rock slope affected by frequency and amplitude of the input motions.

454 **Fig. 12. The absolute difference percentage (Δa) between accelerometer A19 and**
455 **A18**

456 **4.1 Wide frequency effect**

457 Previous studies concluded that frequency had significant effect on dynamic
458 response characteristics of the slope (Geli et al., 1988; Ashford et al., 1997; Del Gaudio
459 and Wasowski, 2007) and the general considered frequencies of engineering interest
460 were between 0.1 and 10 Hz (Ashford et al., 1997; Hailemikael et al., 2016). Based on
461 similarity theorems, the loading frequencies are frequently larger than 50 Hz.
462 Nevertheless, many shaking table tests merely covered a narrow frequency range due
463 to limitation of shaking table capacity (Liu et al., 2013; Srilatha et al., 2013; Liu et al.,
464 2014). Results also indicated that the input frequencies were below or far below the
465 resonance frequencies of the models. In this study, the input frequencies are between
466 15 and 75 Hz which exceed the resonance frequency of the model. Through similarity
467 ratio illustrated in Table 3, the simulated frequencies are 1.5 to 7.5 Hz involved the
468 majority range of engineering interests. Fig. 13 shows the transfer function of several
469 accelerometers under WN1 excitation. It can be determined that resonance frequency
470 in X direction is about 61.24 Hz and vertical direction is around 79.68 Hz.

471 **Fig. 13. Transfer function curve obtained from first excitation of white noise: (a)**
472 **X direction and (b) Z direction**

473 The ground motion of the slope in horizontal X direction increases with the
474 increasing of frequency when the excitation frequency is smaller than 60 Hz, as shown
475 in Fig. 4. Nonetheless, the seismic response in X direction decreases when the
476 frequency is near or greater than resonance frequency. This phenomenon can also be
477 confirmed through the slope surface accelerometers records, as shown in Fig. 14.

478 Interestingly, it can be found that the AAF-X no longer increases with the increasing of
479 χ but decreases first then increases, when the frequency is near or greater than resonance
480 frequency. Yet, previous studies showed that acceleration amplification coefficient still
481 kept an increase trend with the increasing of height when the frequency was near the
482 resonance frequency (Liu et al., 2014; Srilatha et al., 2013). Hence, the slope geometry
483 has a selective seismic response amplification, that is, the ground motion will be
484 amplified at the crest if the frequency of the excitation motion is smaller than the
485 intrinsic vibration frequency of the slope. Generally, the AAF-X should exhibit
486 intensively with frequency 60 Hz which is nearest to resonance frequency in this study.
487 However, the frequency triggered strongest dynamic response is 45 Hz. This difference
488 can be construed in time-frequency domain energy view (Fan et al., 2017). Due to the
489 servo control mode in the experiment, input energy distributes in a wide frequency
490 range when the frequency is 60 and 75 Hz. As a result, it leads to weaker dynamic
491 response at higher frequencies.

492 **Fig. 14. The AAF-X under different frequency excitations with amplitude 0.1g**

493 To reveal the dynamic response change law of the step-like slope dependency on
494 frequency, we comprehensively compare with the present study with previous physical
495 modeling studies. Conveniently, the results of acceleration amplification characteristics
496 are normalized as a function of H/λ , that is, the ratio of the slope height (H) to the
497 wavelength of the stress wave (λ) under consideration, proposed by Ashford et al. (1997).
498 If the input motion is earthquake recording, the dominant frequency of the recording is
499 adopted to calculate the λ . The velocity of shear wave propagation through the medium

500 (C_s) is assumed based on description of the material when the parameter is not presented
501 in references. Hence, results of previous studies (Chen et al., 2010; Dong et al., 2011;
502 Fan et al., 2015; Fan et al., 2016; Lin and Wang, 2006; Liu et al., 2014; Wang, 2006;
503 Xu et al., 2008; Yang et al., 2018a; Yang et al., 2012a; Yang et al., 2012b; Zhao et al.,
504 2015) and this study are shown in Fig. 15. It can be found that acceleration amplification
505 factor at the crest of the slope increases firstly and then it shows a decrease tendency
506 with the increasing H/λ , and the turning value of H/λ is around 0.2 which is also
507 consistent with the numerical simulation results (Ashford et al., 1997; Bouckovalas and
508 Papadimitriou, 2005; Qi, 2006). Also, rock mass structure and dip of the slopes have an
509 influence on value of AAF-X.

510 **Fig. 15. The AAF-X for different physical models with normalized parameter H/λ**

511 **4.2 Excitation amplitude effect**

512 The determined resonance frequency and calculated damping ratio in X direction
513 under different WN excitation stages are shown in Fig. 16(a). It can be found that the
514 resonance frequency at upper surface of the slope increases as the excitation amplitude
515 increasing. At the same time, the damping ratio at the same location shows an increasing
516 trend. Moreover, Fig 16(b) indicates that AAF-X increase with the increasing of χ when
517 the excitation amplitude is below 0.4 g, while AAF-X decreases firstly and then
518 increases as the amplitude reaches 0.5 g. Here, we also calculate the shear stress-strain
519 in different location of the slope adopting the method in references (Zeghal et al., 1995;
520 Zeghal et al., 1999) and it is also widely used in shaking table test (Brennan et al., 2005;
521 Su et al., 2021). The stress can be evaluated by the first-order linear interpolation of the

522 monitoring accelerations along a vertical section and strains are obtained by second-
523 order interpolation between displacements. The stress-strain of the corresponding point
524 between A04 and A15 (see Fig. 3) is shown in Fig. 17. It can be found that the equivalent
525 shear modulus has a decrease tendency with the increasing of input amplitudes.

526 **Fig. 16. Resonance frequency and damping ratio under different WN stages**

527 **Fig. 17. Shear stress-strain histories of the corresponding point between A04 and**
528 **A15 under different amplitude excitation with frequency of 15 Hz**

529 Hence, the excitation amplitude of the earthquake will affect the seismic response
530 of the slope in two ways. On one hand, the geometry amplification results in AAF-X
531 amplification along the slope surface especially at the slope crest. As a result, the
532 stronger the acceleration intensity, the more severe the deterioration of the slope
533 material (see Fig. 17) and the larger damping ratio of the slope (see Fig. 16b). On the
534 other hand, increasing damping ratio and weaker structure will dissipate more energy,
535 which may result in decreasing of the acceleration amplification. In current study, the
536 acceleration ground motion amplification was stronger than system energy dissipation
537 when the excitation amplitude is between 0.1 g and 0.4 g. Hence, the AAF-X shows an
538 amplification trend along the slope surface. Nevertheless, when the excitation
539 amplitude is up to 0.5 g, the energy dissipation of the slope material or structure was
540 larger than acceleration amplification, which lead to decrease of the AAF-X, as shown
541 in Fig. 18. It can be also found that damping ratio of the material increased rapidly when
542 the excitation amplitude reaches 0.3 g which indicating initiation of a nonlinear
543 dynamic response.

544 Therefore, whether dynamic response of a slope amplifies or not depends on
545 relationship between input motion characteristics (including the amplitude and
546 frequency) and weakening degree of the slope.

547 **Fig. 18. The AAF-X of surface accelerometers under increase of amplitude**
548 **excitation with frequency of 15 Hz**

549 **4.3 Implications to engineering application**

550 As aforementioned results, ground motion in horizontal direction amplified at the
551 slope surface near the slope crest while vertical direction dominated at lower part of the
552 slope. However, only a few seismic codes (EC-8 and AFPS) propose to consider
553 topography amplification in horizontal direction, let alone parasitic vertical
554 amplification. Hence, infrastructures like power supply pylons construction should be
555 taken into account acceleration amplification in horizontal and vertical direction in high
556 seismic intensity mountain area, like south-west of China. Furthermore, much works
557 should be taken in depth to obtain seismic parameters for code design.

558 **5 Conclusions**

559 In current study, seismic response of a step-like homogeneous rock slope was
560 investigated using a large-scale shaking table test. Then, a series of shaking table tests
561 were subjected to harmonic shear loads with wide frequency and amplitude. The
562 accelerations at the surface and inside of the slope were measured and seismic response
563 change law of the slope was discussed. Some conclusions can be reached as follows:

564 (1) The AAF-X shows an increasing trend along the slope surface with the
565 elevation increasing and amplifies dramatically at the slope crest under smaller

566 amplitude. Nevertheless, the AAF-Z increases firstly and then decreases and amplifies
567 strongest at surface of the slope near the toe.

568 (2) The AAF-X and AAF-Z depend on the loading frequencies. The AAF-X near
569 the slope crest increases firstly and then decreases while the AAF-Z shows an increasing
570 trend, with the increasing of input motion frequencies under same amplitude excitation.
571 Seismic response of the slopes shows strongest amplification when H/λ is around 0.2
572 and AAF-X exhibits a decrease trend when H/λ is larger than 0.2.

573 (3) Dynamic response of the slope shows an increasing trend first and then
574 decreases as the input amplitude increasing. Resonance frequency and damping ratio
575 and shear stress-strain curve indicate amplitude has a “double-effect” effect on the
576 seismic characteristics of the slope. If the energy dissipation of the slope material or
577 structure was larger than acceleration amplification, nonlinear dynamic response of the
578 slope under earthquake will be occurred.

579 **Acknowledgements**

580 This research was funded by the National Natural Science Foundation of China
581 (grants number of 41825018, 41672307 and 41790442) and the Second Tibetan Plateau
582 Scientific Expedition and Research Program (STEP) under grant of No.
583 2019QZKK0904.

584 **References**

585 Ashford, S.A., Sitar, N., Lysmer, J. & Deng, N. 1997. Topographic effects on the
586 seismic response of steep slopes. *Bulletin of the Seismological Society of America*,
587 **87**, 701-709.

588 Bouckovalas, G.D. & Papadimitriou, A.G. 2005. Numerical evaluation of slope
589 topography effects on seismic ground motion. *Soil Dynamics and Earthquake*
590 *Engineering*, **25**, 547-558, doi: 10.1016/j.solidyn.2004.11.008.

591 Brand, L. 1957. The Pi-theorem of dimensional analysis. *Archive for Rational*
592 *Mechanics and Analysis*, **1**, 35-45, doi: 10.1007/bf00297994.

593 Brennan, A.J., Thusyanthan, N.I. & Madabhushi, S.P.G. 2005. Evaluation of shear
594 modulus and damping in dynamic centrifuge tests. *Journal of geotechnical and*
595 *geoenvironmental engineering*, **131**, 1488-1497, doi: 10.1061/(asce)1090-
596 0241(2005)131:12(1488).

597 Chen, X., Shen, J., Wei, P. & Yang, J. 2010. Large-scale Shaking Table Test of Seismic
598 Stability of Xiashu Loess Slopes: Analysis of Test Results(II). *Journal of Disaster*
599 *Prevention and Mitigation Engineering*, **30**, 587-594.

600 Davis, L.L. & West, L.R. 1973. Observed effects of topography on ground motion.
601 *Bulletin of the Seismological Society of America*, **63**, 283-298.

602 Del Gaudio, V. & Wasowski, J. 2007. Directivity of slope dynamic response to seismic
603 shaking. *Geophysical Research Letters*, **34**, L12301, doi: 10.1029/2007gl029842.

604 Dong, J., Yang, G., Wu, F. & Qi, S. 2011. The large-scale shaking table test study of
605 dynamic response and failure mode of bedding rock slope under earthquake. *Rock*
606 *and Soil Mechanics*, **32**, 2977-2982.

607 Fan, G., Zhang, J., Fu, X., Du, L. & Liu, F. 2015. Large-scale shaking table test on
608 dynamic response of bedding rock slopes with silt intercalation. *Chinese Journal*
609 *of Rock Mechanics and Engineering*, **34**, 1750-1757.

610 Fan, G., Zhang, J.J., Wu, J.B. & Yan, K.M. 2016. Dynamic Response and Dynamic
611 Failure Mode of a Weak Intercalated Rock Slope Using a Shaking Table. *Rock*
612 *Mechanics and Rock Engineering*, **49**, 3243-3256, doi: 10.1007/s00603-016-
613 0971-7.

614 Fan, G., Zhang, L.M., Zhang, J.J. & Yang, C.W. 2017. Time-frequency analysis of
615 instantaneous seismic safety of bedding rock slopes. *Soil Dynamics and*
616 *Earthquake Engineering*, **94**, 92-101, doi: 10.1016/j.soildyn.2017.01.008.

617 Geli, L., Bard, P.Y. & Jullien, B. 1988. The effect of topography on earthquake ground
618 motion - a review and new results. *Bulletin of the Seismological Society of*
619 *America*, **78**, 42-63.

620 Guo, S.F., Qi, S.W., Yang, G.X., Zhang, S.S. & Saroglou, C. 2017. An Analytical
621 Solution for Block Toppling Failure of Rock Slopes during an Earthquake. *Applied*
622 *Sciences-Basel*, **7**, 17, doi: 10.3390/app7101008.

623 Hailemikael, S., Lenti, L., Martino, S., Paciello, A., Rossi, D. & Mugnozza, G.S. 2016.
624 Ground-motion amplification at the Colle di Roio ridge, central Italy: a combined
625 effect of stratigraphy and topography. *Geophysical Journal International*, **206**, 1-
626 18, doi: 10.1093/gji/ggw120.

627 Hartzell, S.H., Carver, D.L. & King, K.W. 1994. Initial investigation of site and
628 topographic effects at Robinwood ridge, California. *Bulletin of the Seismological*
629 *Society of America*, **84**, 1336-1349.

630 He, J., Qi, S., Wang, Y. & Saroglou, C. 2020. Seismic response of the Lengzhuguan
631 slope caused by topographic and geological effects. *Engineering Geology*, **265**,
632 105431, doi: <https://doi.org/10.1016/j.enggeo.2019.105431>.

633 He, J., Qi, S., Zhan, Z., Guo, S., Li, C., Zheng, B., Huang, X., Zou, Y., Yang, G. &
634 Liang, N. 2021. Seismic response characteristics and deformation evolution of the
635 bedding rock slope using a large-scale shaking table. *Landslides*, doi:
636 10.1007/s10346-021-01682-w.

637 Hough, S.E., Altidor, J.R., Anglade, D., Given, D., Janvier, M.G., Maharrey, J.Z.,
638 Meremonte, M., Mildor, B.S., Prepetit, C. & Yong, A. 2010. Localized damage
639 caused by topographic amplification during the 2010 M 7.0 Haiti earthquake.
640 *Nature Geoscience*, **3**, 778-782, doi: 10.1038/ngeo988.

641 Iai, S. 1989. Similitude for shaking table tests on soil-structure-fluid model in 1g
642 gravitational field. *Soils and Foundations*, **29**, 105-118.

643 Jiang, L., Yao, L., Wu, W. & Xu, G. 2010. Transfer function analysis of earthquake
644 simulation shaking table model test of side slopes. *Rock and Soil Mechanics*, **31**,
645 1368-1374.

- 646 Khazai, B. & Sitar, N. 2004. Evaluation of factors controlling earthquake-induced
647 landslides caused by Chi-Chi earthquake and comparison with the Northridge and
648 Loma Prieta events. *Engineering Geology*, **71**, 79-95, doi: 10.1016/s0013-
649 7952(03)00127-3.
- 650 Lin, M.L. & Wang, K.L. 2006. Seismic slope behavior in a large-scale shaking table
651 model test. *Engineering Geology*, **86**, 118-133, doi: 10.1016/j.enggeo.2006.02.011.
- 652 Liu, H.X., Xu, Q. & Li, Y.R. 2014. Effect of lithology and structure on seismic response
653 of steep slope in a shaking table test. *Journal of Mountain Science*, **11**, 371-383,
654 doi: 10.1007/s11629-013-2790-6.
- 655 Liu, H.X., Xu, Q., Li, Y.R. & Fan, X.M. 2013. Response of High-Strength Rock Slope
656 to Seismic Waves in a Shaking Table Test. *Bulletin of the Seismological Society
657 of America*, **103**, 3012-3025, doi: 10.1785/0120130055.
- 658 Luo, Y.H., Del Gaudio, V., Huang, R.Q., Wang, Y.S. & Wasowski, J. 2014. Evidence of
659 hillslope directional amplification from accelerometer recordings at Qiaozhuang
660 (Sichuan - China). *Engineering Geology*, **183**, 193-207, doi:
661 10.1016/j.enggeo.2014.10.015.
- 662 Owen, L.A., Kamp, U., Khattak, G.A., Harp, E.L., Keefer, D.K. & Bauer, M.A. 2008.
663 Landslides triggered by the 8 October 2005 Kashmir earthquake. *Geomorphology*,
664 **94**, 1-9, doi: 10.1016/j.geomorph.2007.04.007.
- 665 Qi, S., Xu, Q., Lan, H., Zhang, B. & Liu, J. 2010. Spatial distribution analysis of
666 landslides triggered by 2008.5. 12 Wenchuan Earthquake, China. *Engineering
667 Geology*, **116**, 95-108.
- 668 Qi, S.W. 2006. Two patterns of dynamic responses of single-free-surface slopes and
669 their threshold height. *Chinese Journal of Geophysics-Chinese Edition*, **49**, 518-
670 523.
- 671 Qi, S.W., Wu, F.Q. & Sun, J.Z. 2003. General regularity of dynamic responses of slopes
672 under dynamic input. *Science in China Series E-Engineering & Materials Science*,
673 **46**, 120-132, doi: 10.1360/03ez0006.
- 674 Sepulveda, S.A., Murphy, W. & Petley, D.N. 2005. Topographic controls on coseismic

675 rock slides during the 1999 Chi-Chi earthquake, Taiwan. Quarterly journal of
676 engineering geology and hydrogeology, **38**, 189-196, doi: 10.1144/1470-9236/04-
677 062.

678 Shi, Z.M., Wang, Y.Q., Peng, M., Chen, J.F. & Yuan, J. 2015a. Characteristics of the
679 landslide dams induced by the 2008 Wenchuan earthquake and dynamic behavior
680 analysis using large-scale shaking table tests. Engineering Geology, **194**, 25-37,
681 doi: 10.1016/j.enggeo.2014.10.009.

682 Shi, Z.M., Wang, Y.Q., Peng, M., Guan, S.G. & Chen, J.F. 2015b. Landslide dam
683 deformation analysis under aftershocks using large-scale shaking table tests
684 measured by videogrammetric technique. Engineering Geology, **186**, 68-78, doi:
685 10.1016/j.enggeo.2014.09.008.

686 Song, D.Q., Che, A.L., Chen, Z. & Ge, X.R. 2018a. Seismic stability of a rock slope
687 with discontinuities under rapid water drawdown and earthquakes in large-scale
688 shaking table tests. Engineering Geology, **245**, 153-168, doi:
689 10.1016/j.enggeo.2018.08.011.

690 Song, D.Q., Che, A.L., Zhu, R.J. & Ge, X.R. 2018b. Dynamic response characteristics
691 of a rock slope with discontinuous joints under the combined action of earthquakes
692 and rapid water drawdown. Landslides, **15**, 1109-1125, doi: 10.1007/s10346-017-
693 0932-6.

694 Srilatha, N., Latha, G.M. & Puttappa, C.G. 2013. Effect of frequency on seismic
695 response of reinforced soil slopes in shaking table tests. Geotextiles and
696 Geomembranes, **36**, 27-32, doi: 10.1016/j.geotexmem.2012.10.004.

697 Su, L., Li, C. & Zhang, C. 2021. Large-scale shaking table tests on the seismic
698 responses of soil slopes with various natural densities. Soil Dynamics and
699 Earthquake Engineering, **140**, 106409, doi:
700 <https://doi.org/10.1016/j.soildyn.2020.106409>.

701 Tucker, B.E., King, J.L., Hatzfeld, D. & Nersesov, I.L. 1984. Observations of hard-rock
702 site effects. Bulletin of the Seismological Society of America, **74**, 121-136.

703 Wang, G. 2006. *Development of Regional Seismic Slope Analysis Model Based on the*

704 *Cases of Chi-Chi Earthquake*. PhD thesis, National Taiwan University.

705 Wang, K.L. & Lin, M.L. 2011. Initiation and displacement of landslide induced by
706 earthquake - a study of shaking table model slope test. *Engineering Geology*, **122**,
707 106-114, doi: 10.1016/j.enggeo.2011.04.008.

708 Wang, Y.S., He, J.X. & Luo, Y.H. 2017. Seismic response of the Lengzhuguan slope
709 during Kangding Ms5.8 earthquake. *Journal of Mountain Science*, **14**, 2337-2347,
710 doi: 10.1007/s11629-017-4368-1.

711 Wartman, J., Seed, R.B. & Bray, J.D. 2005. Shaking table modeling of seismically
712 induced deformations in slopes. *Journal of geotechnical and geoenvironmental*
713 *engineering*, **131**, 610-622, doi: 10.1061/(asce)1090-0241(2005)131:4(610).

714 Xu, G., Yao, L., Gao, Z. & Li, Z. 2008. Large-scale shaking table model test study on
715 dynamic characteristics and dynamic responses of slope. *Chinese Journal of Rock*
716 *Mechanics and Engineering*, **27**, 624-632.

717 Yang, B., Yang, X., Yang, T., WANG, R. & ZHOU, D. 2018a. Shaking table model test
718 on dynamic response and failure process of shatter-burst sliding slope under
719 earthquake load. *Chinese Journal of Rock Mechanics and Engineering*, **37**, 3279-
720 3290.

721 Yang, G., Qi, S., Wu, F. & Zhan, Z. 2018. Seismic amplification of the anti-dip rock
722 slope and deformation characteristics: A large-scale shaking table test. *Soil*
723 *Dynamics and Earthquake Engineering*, **115**, 907-916, doi:
724 <https://doi.org/10.1016/j.soildyn.2017.09.010>.

725 Yang, G., Wu, F., Dong, J. & Qi, S. 2012. Study of dynamic response characters and
726 failure mechanism of rock slope under earthquake. *Chinese Journal of Rock*
727 *Mechanics and Engineering*, **31**, 696-702.

728 Yang, G., Ye, H., Wu, F., Qi, S. & Dong, J. 2012. Shaking table model test on dynamic
729 response characteristics and failure mechanism of antidip layered rock slope.
730 *Chinese Journal of Rock Mechanics and Engineering*, **31**, 2214-2221.

731 Yin, Y.P., Wang, F.W. & Sun, P. 2009. Landslide hazards triggered by the 2008
732 Wenchuan earthquake, Sichuan, China. *Landslides*, **6**, 139-152, doi:

733 10.1007/s10346-009-0148-5.

734 Zeghal, M., Elgamal, A.W., Tang, H.T. & Stepp, J.C. 1995. Lotung downhole array .2.
735 evaluation of soil nonlinear properties. Journal of Geotechnical Engineering-Asce,
736 **121**, 363-378, doi: 10.1061/(asce)0733-9410(1995)121:4(363).

737 Zeghal, M., Elgamal, A.W., Zeng, X.W. & Arulmoli, K. 1999. Mechanism of
738 liquefaction response in sand-silt dynamic centrifuge tests. Soil Dynamics and
739 Earthquake Engineering, **18**, 71-85, doi: 10.1016/s0267-7261(98)00029-3.

740 Zhan, Z., Qi, S., He, N., Zheng, B. & Ge, C. 2019. Shaking table test study of
741 homogeneous rock slope model under strong earthquake. Journal of Engineering
742 Geology, **27**, 946-954.

743 Zhao, M.S., Huang, D., Cao, M.S. & Qiao, J.P. 2015. Shaking table tests on deformation
744 and failure mechanisms of seismic slope. Journal of Vibroengineering, **17**, 382-
745 392.

746 **Table list (Total of 5)**

747 **Table 1 The dimension factor of the variables adopted in shaking table test**

	l	ρ	a	c	φ	E	μ	σ_c	σ_i	σ	ε	u	v	g	ω	t
	a_1	a_2	a_3	a_4	a_5	a_6	a_7	a_8	a_9	a_{10}	a_{11}	a_{12}	a_{13}	a_{14}	a_{15}	a_{16}
[M]	0	1	0	1	0	1	0	1	1	1	0	0	0	0	0	0
[L]	1	-3	1	-1	0	-1	0	-1	-1	-1	0	1	1	1	0	0
[T]	0	0	-2	-2	0	-2	0	-2	-2	-2	0	0	-1	-2	-1	1

748 $*a_i$ represents the exponential term i -th parameter.

749

Table 2 The similarity criterion in the shaking table test

	<i>c</i>	φ	<i>E</i>	μ	σ_c	σ_t	σ	ε	<i>u</i>	<i>v</i>	<i>g</i>	ω	<i>t</i>	<i>l</i>	ρ	<i>a</i>	Similarity
	<i>a4</i>	<i>a5</i>	<i>a6</i>	<i>a7</i>	<i>a8</i>	<i>a9</i>	<i>a10</i>	<i>a11</i>	<i>a12</i>	<i>a13</i>	<i>a14</i>	<i>a15</i>	<i>a16</i>	<i>a1</i>	<i>a2</i>	<i>a3</i>	criterion
π_1	1	0	0	0	0	0	0	0	0	0	0	0	0	-1	-1	-1	$C_c=C_l C_\rho C_a$
π_2		1	0	0	0	0	0	0	0	0	0	0	0	0	0	0	1
π_3			1	0	0	0	0	0	0	0	0	0	0	-1	-1	-1	$C_E=C_l C_\rho C_a$
π_4				1	0	0	0	0	0	0	0	0	0	0	0	0	1
π_5					1	0	0	0	0	0	0	0	0	-1	-1	-1	$C_{\sigma_c}=C_l C_\rho C_a$
π_6						1	0	0	0	0	0	0	0	-1	-1	-1	$C_{\sigma_t}=C_l C_\rho C_a$
π_7							1	0	0	0	0	0	0	-1	-1	-1	$C_\sigma=C_l C_\rho C_a$
π_8								1	0	0	0	0	0	0	0	0	1
π_9									1	0	0	0	0	-1	0	0	$C_u=C_l$
π_{10}										1	0	0	0	-1/2	0	-1/2	$C_v=C_l^{1/2} C_a^{1/2}$
π_{11}											1	0	0	0	0	-1	$C_g=C_a$
π_{12}												1	0	1/2	0	-1/2	$C_\omega=C_l^{1/2} C_a^{-1/2}$
π_{13}													1	-1/2	0	1/2	$C_t=C_l^{1/2} C_a^{-1/2}$

Table 3 The similarity ratios of considered parameters

Parameters	Dimensionless π term	Similarity ratio	Parameters	Dimensionless π term	Similarity ratio
l	Fundamental quantity	$C_l=100$	σ_t	$C_{\sigma_t}=C_l C_\rho C_a$	$C_{\sigma_t}=100$
ρ	Fundamental quantity	$C_\rho=1$	σ	$C_\sigma=C_l C_\rho C_a$	$C_\sigma=100$
a	Fundamental quantity	$C_a=1$	ε	1	$C_\varepsilon=1$
c	$C_c=C_l C_\rho C_a$	$C_c=100$	u	$C_u=C_l$	$C_u=100$
φ	1	$C_\varphi=1$	v	$C_v=C_l^{1/2} C_a^{1/2}$	$C_v=10$
E	$C_E=C_l C_\rho C_a$	$C_E=100$	g	$C_g=C_a$	$C_g=10$
μ	1	$C_\mu=1$	ω	$C_\omega=C_l^{-1/2} C_a^{-1/2}$	$C_\omega=0.1$
σ_c	$C_{\sigma_c}=C_l C_\rho C_a$	$C_{\sigma_c}=100$	t	$C_t=C_l^{1/2} C_a^{-1/2}$	$C_t=10$

754

Table 4 Parameters of the similarity material

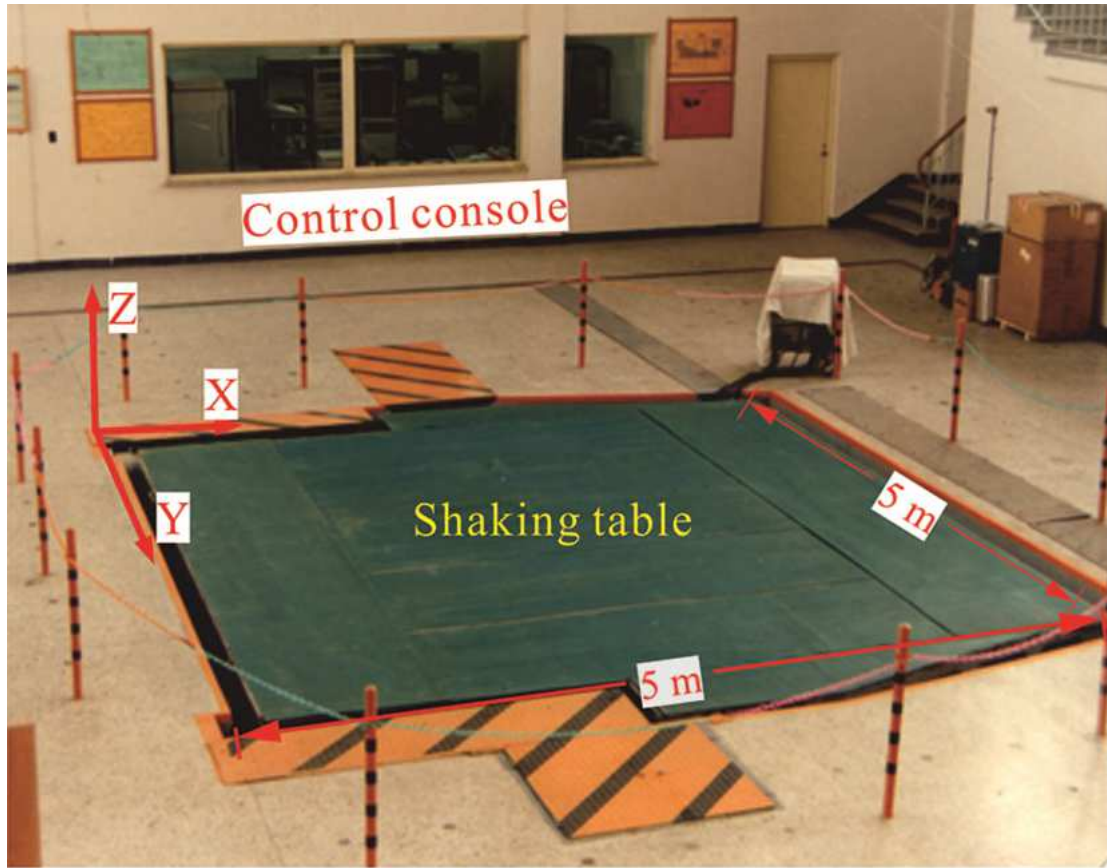
Materials	Density ρ (kg/m ³)	Elasticity modulus E (MPa)	Compression strength σ_c (MPa)	Cohesion c (MPa)	Friction angle φ (°)	Poisson's ratio μ
Similarity	2630	335.52	0.98	0.20	26.76	0.26
Prototype	2630	3.3552×10 ⁴	98	20	26.76	0.26

755

Table 5 The excitation scheme

Excitations	Amplitude (g)	Frequency (Hz)	Durations (s)	Excitations	Amplitude (g)	Frequency (Hz)	Durations (s)
WN1	0.1	0.1-120	90	WN4	0.1	0.1-120	90
		15	10			15	10
		30	10			30	10
Harmonic	0.1	45	10	Harmonic	0.4	45	10
wave		60	10	wave		60	10
		75	10			75	10
WN2	0.1	0.1-120	90	WN5	0.1	0.1-120	90
		15	10			15	10
		30	10			30	10
Harmonic	0.2	45	10	Harmonic	0.5	45	10
wave		60	10	wave		60	10
		75	10			75	10
WN3	0.1	0.1-120	90	WN6	0.1	0.1-120	90
		15	10				
		30	10				
Harmonic	0.3	45	10				
wave		60	10				
		75	10				

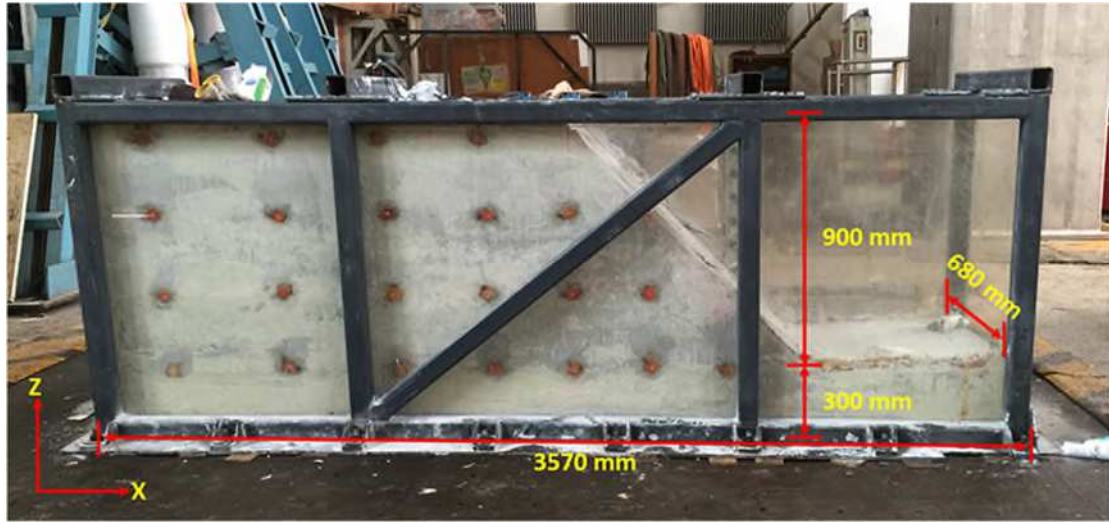
Figure list (Total of 18)



759

760 **Fig. 1** Layout of the shaking table at IWHR

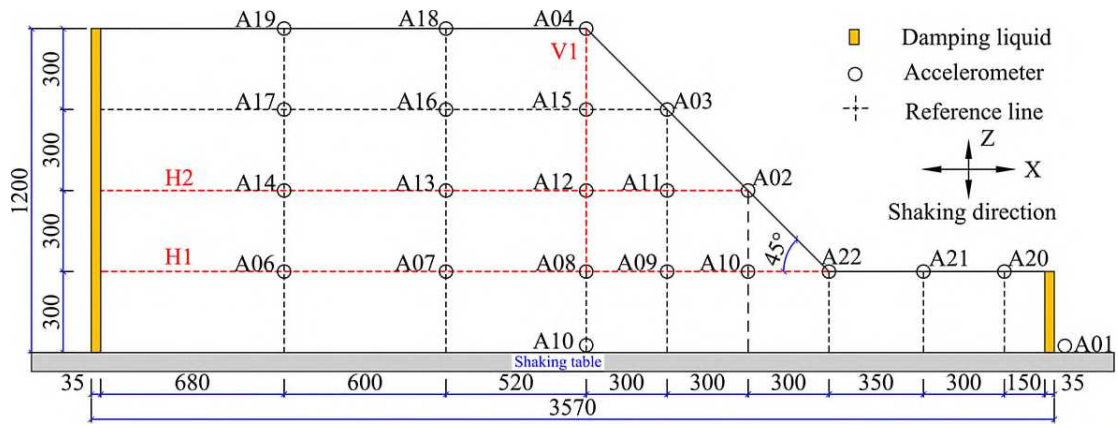
761



762

763 **Fig. 2** The front view of the physical model before test

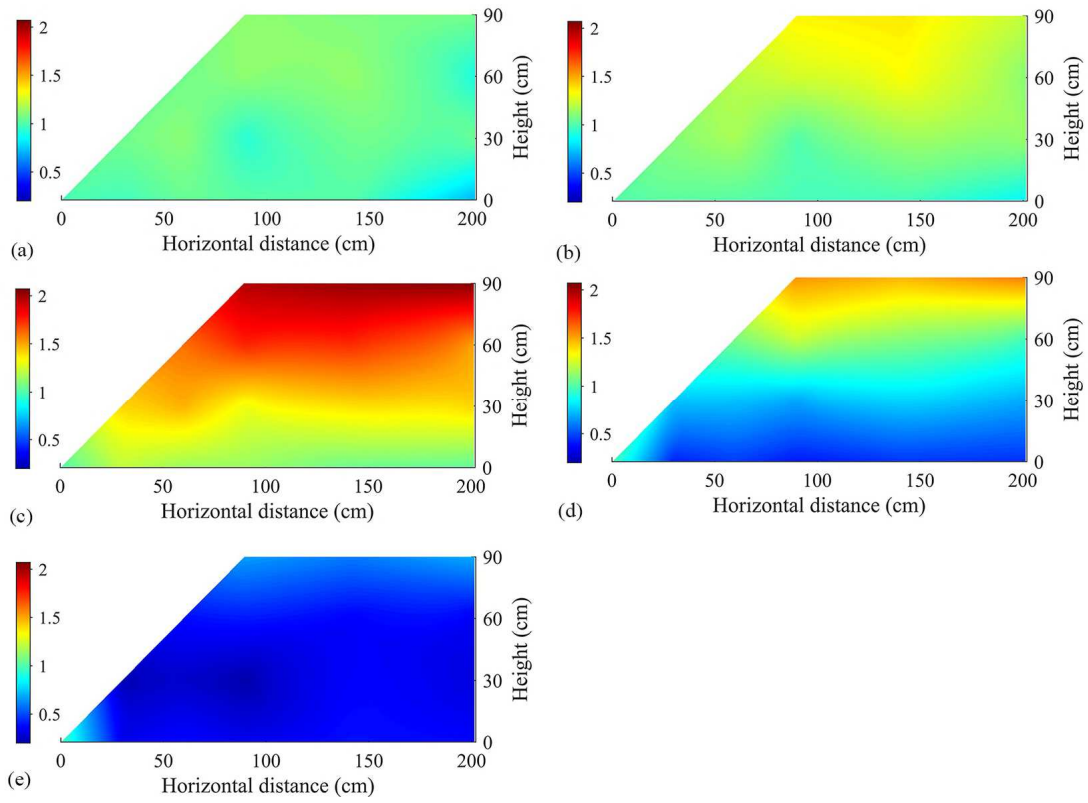
764



765

766 **Fig. 3** Schematic design of the slope model (unit: mm)

767

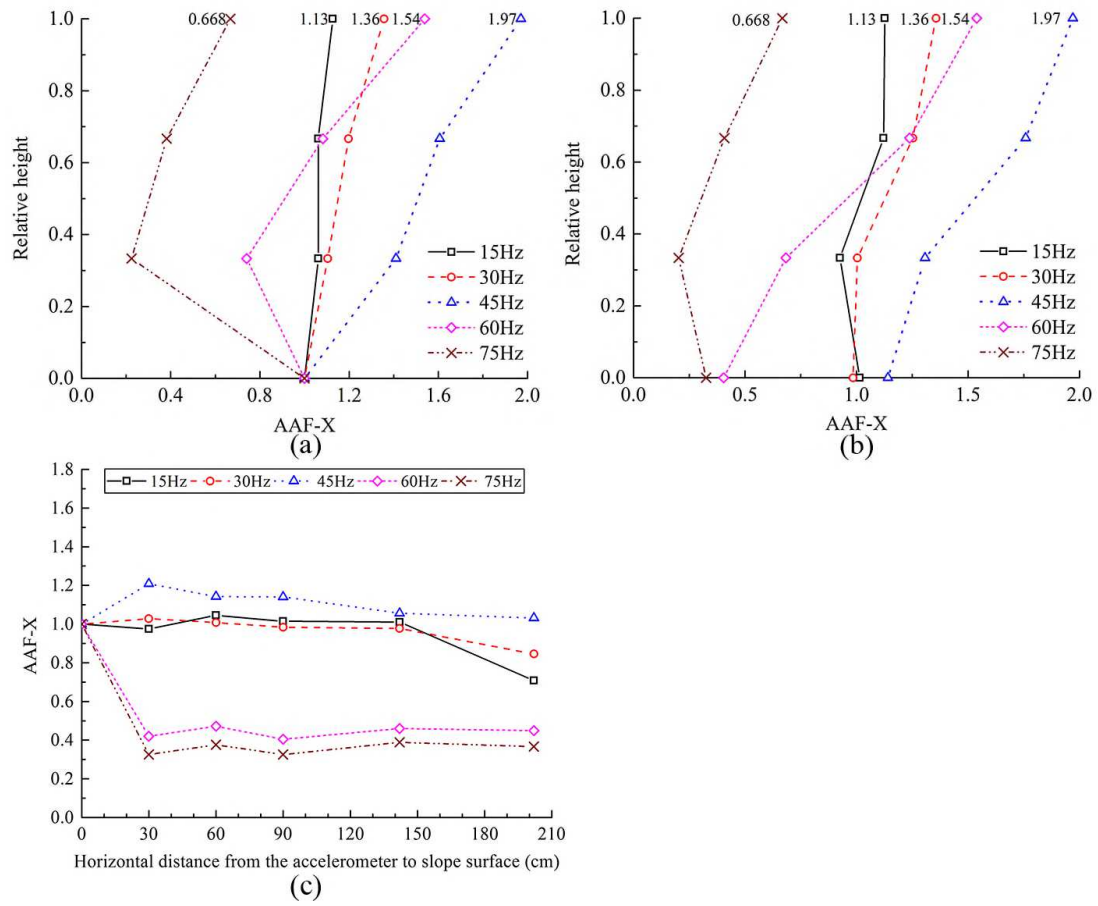


768

769 **Fig. 4** AAF-X distribution along slope section under the excitation amplitude of 0.1g:

770 (a) 15 Hz; (b) 30 Hz; (c) 45 Hz; (d) 60 Hz; (e) 75 Hz

771

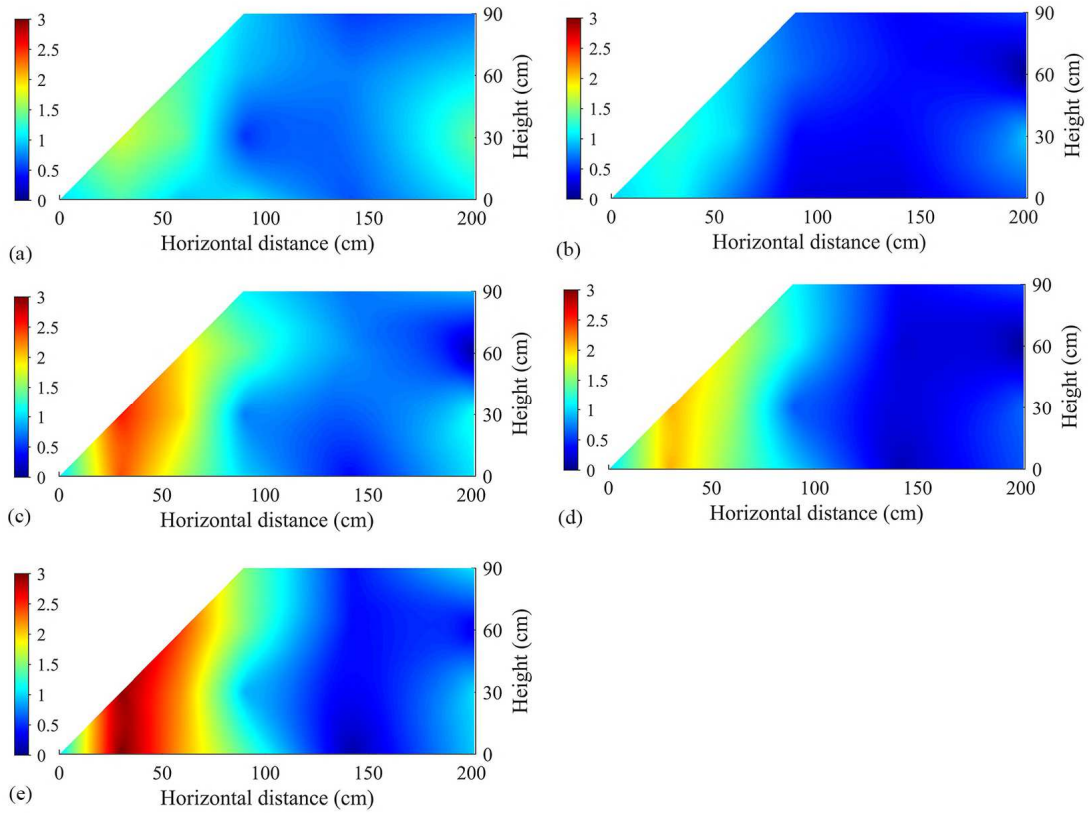


772

773 **Fig. 5** The AAF-X change law of different sections (a) slope surface, (b) V1 and (c) H1

774 under the excitation amplitude of 0.1g

775



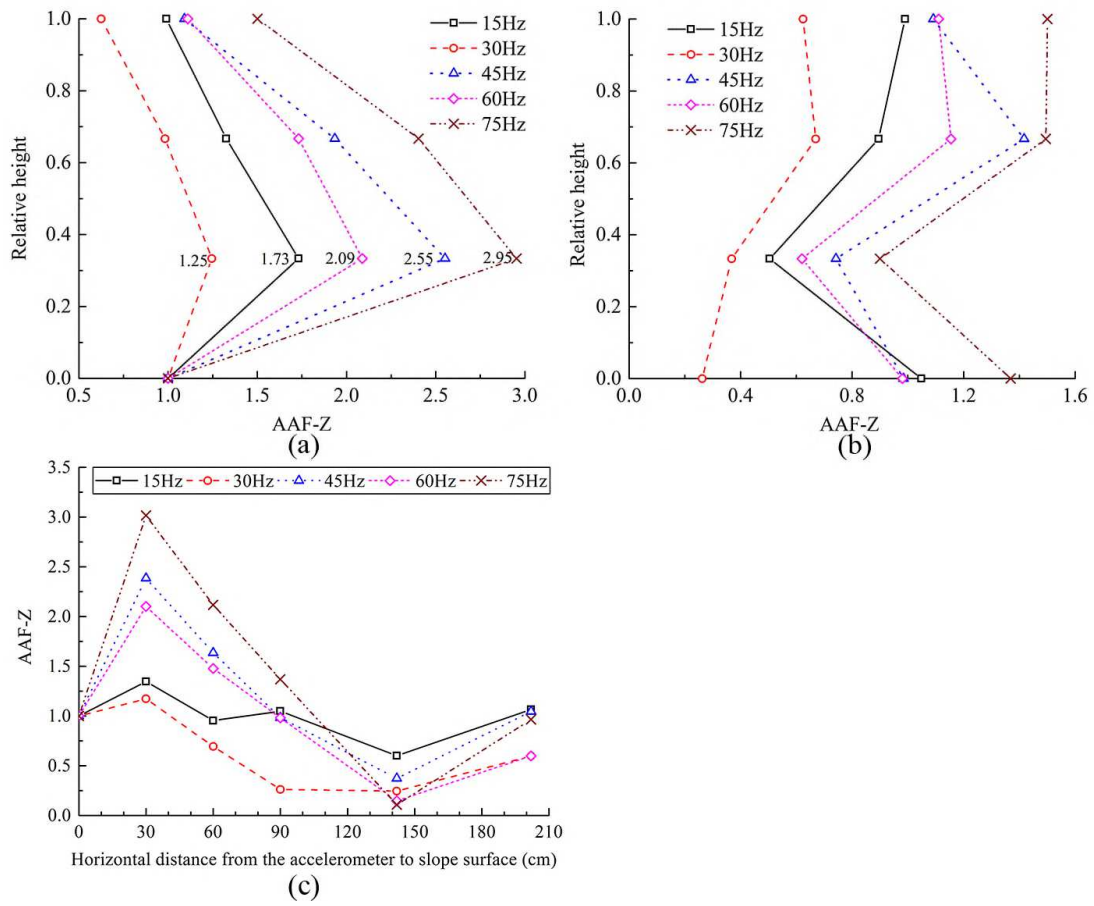
776

777 **Fig. 6.** AAF-Z distribution along the slope section under the excitation amplitude of
 778 0.1g with different frequency: (a) – (e) are from 15 Hz to 75 Hz with an interval of 15

779

Hz

780

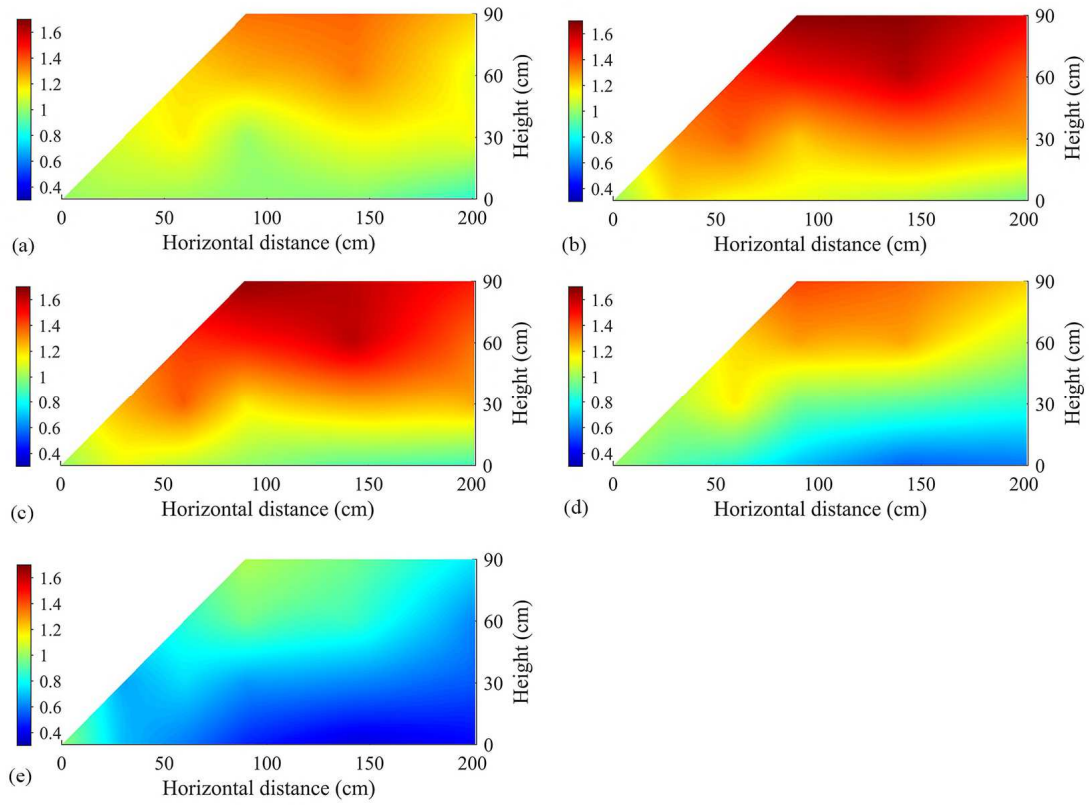


781

782 **Fig. 7** The AAF-Z along the (a) slope surface, (b) H1 and (c) V1 under the excitation

783 amplitude of 0.1g

784

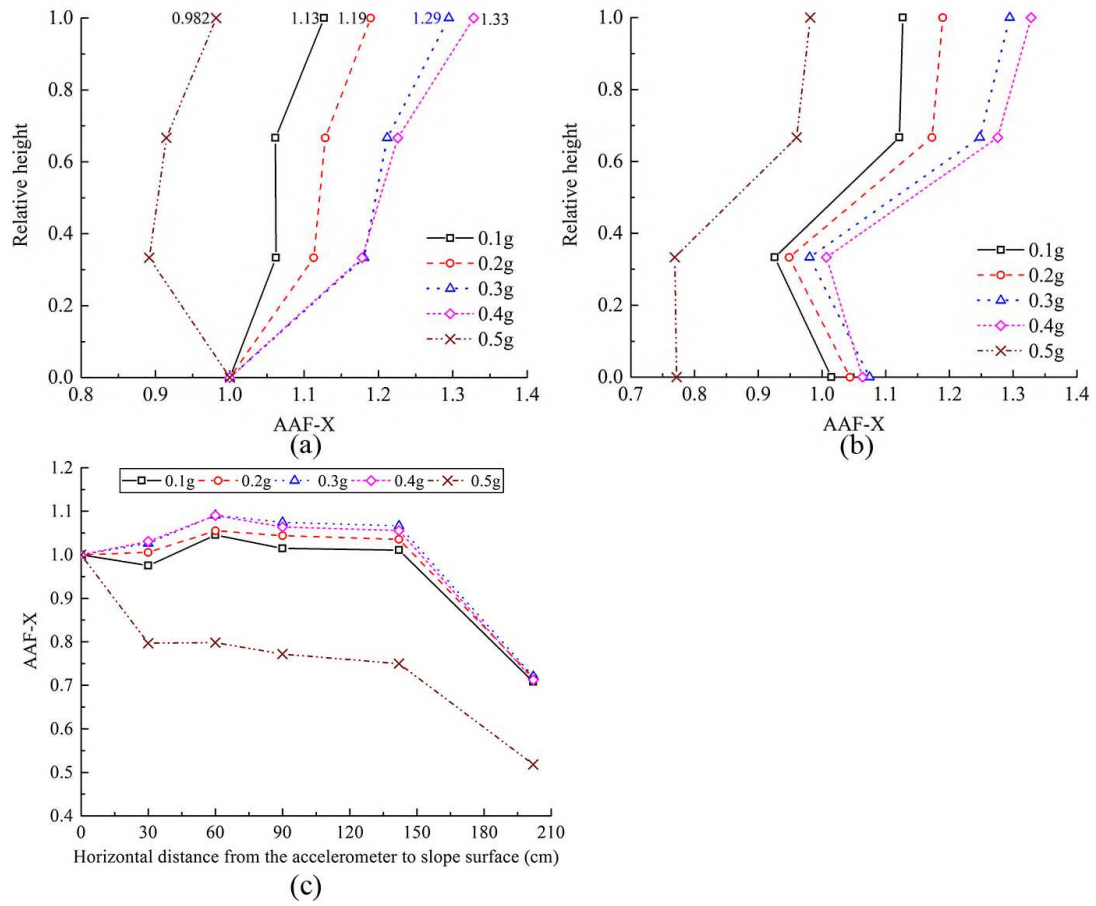


785

786 **Fig. 8.** AAF-X distribution along the slope section under the excitation frequency 15

787 Hz with different amplitude: (a) – (e) are from 0.1 g 0.5 g with an interval of 0.1 g

788

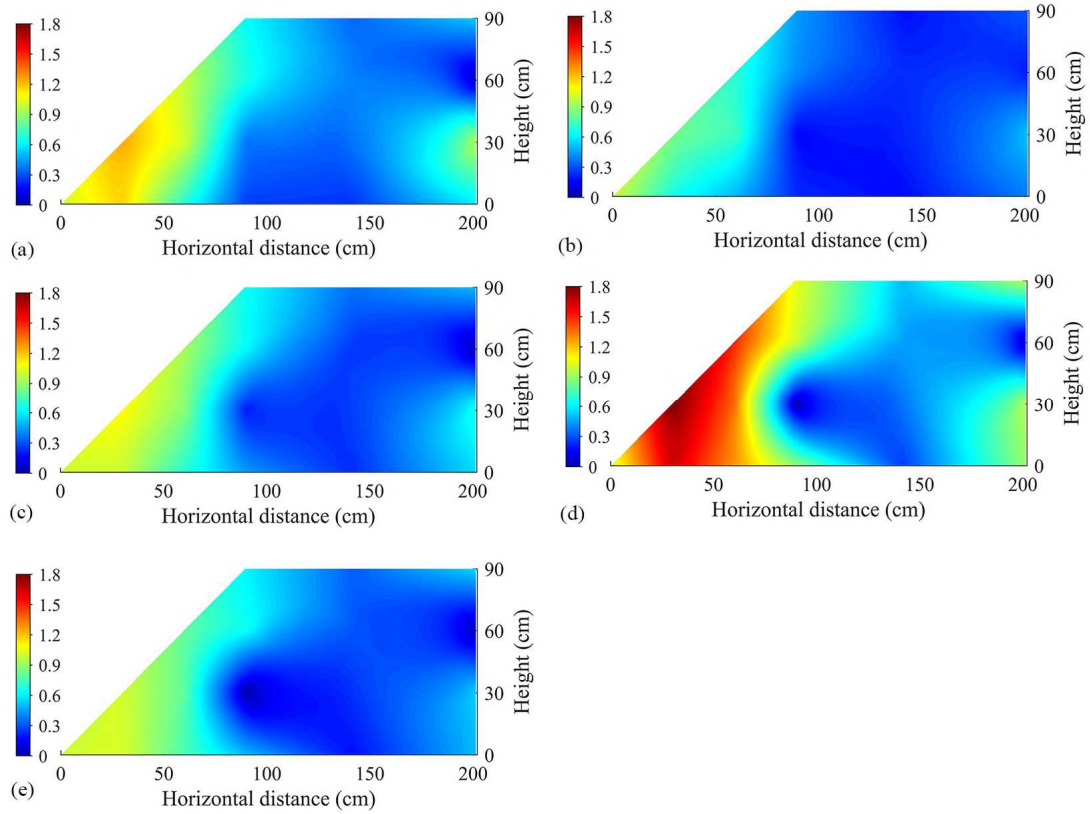


789

790 **Fig. 9** The AAF-X change law of different sections (a) slope surface, (b) H1 and (c) V1

791 under the excitation frequency 15 Hz

792

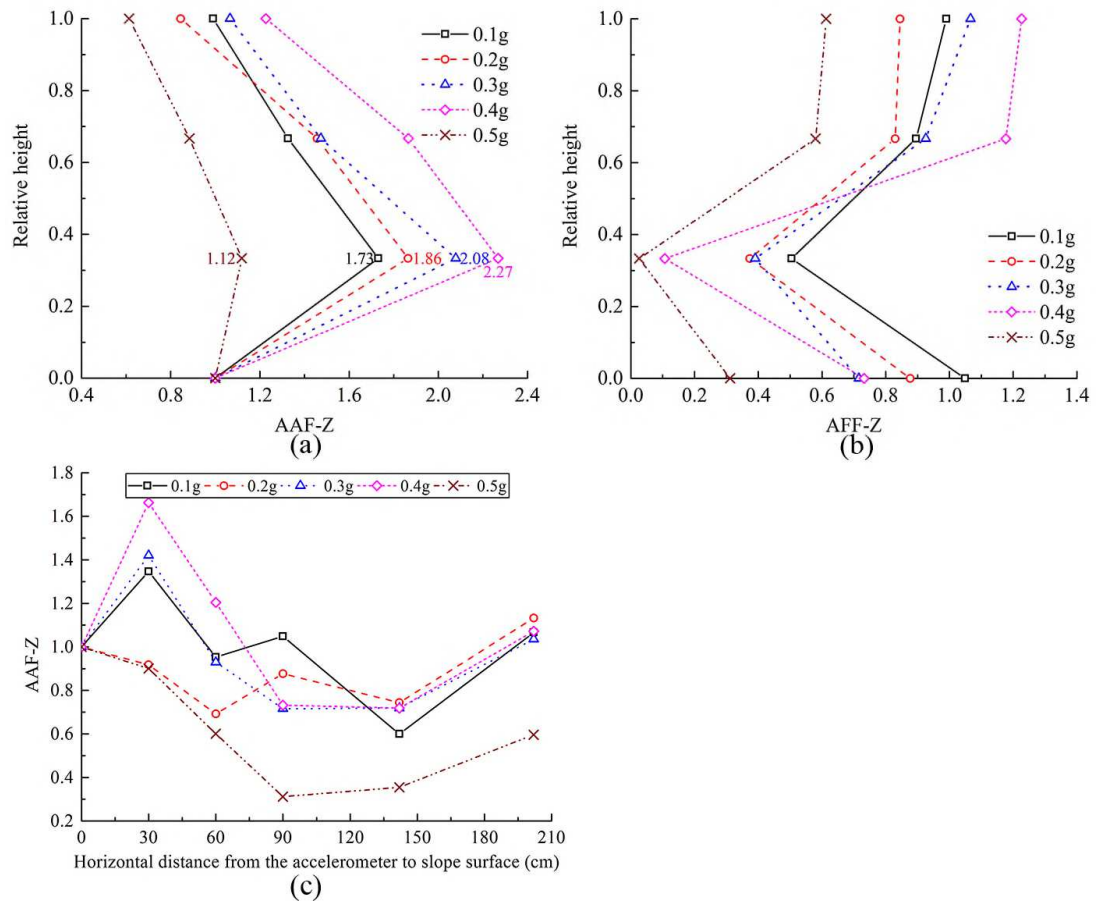


793

794 **Fig. 10.** AAF-X distribution along the slope section under the excitation frequency 15

795 Hz with different amplitude: (a) – (e) are from 0.1 g to 0.5 g with an interval of 0.1 g

796

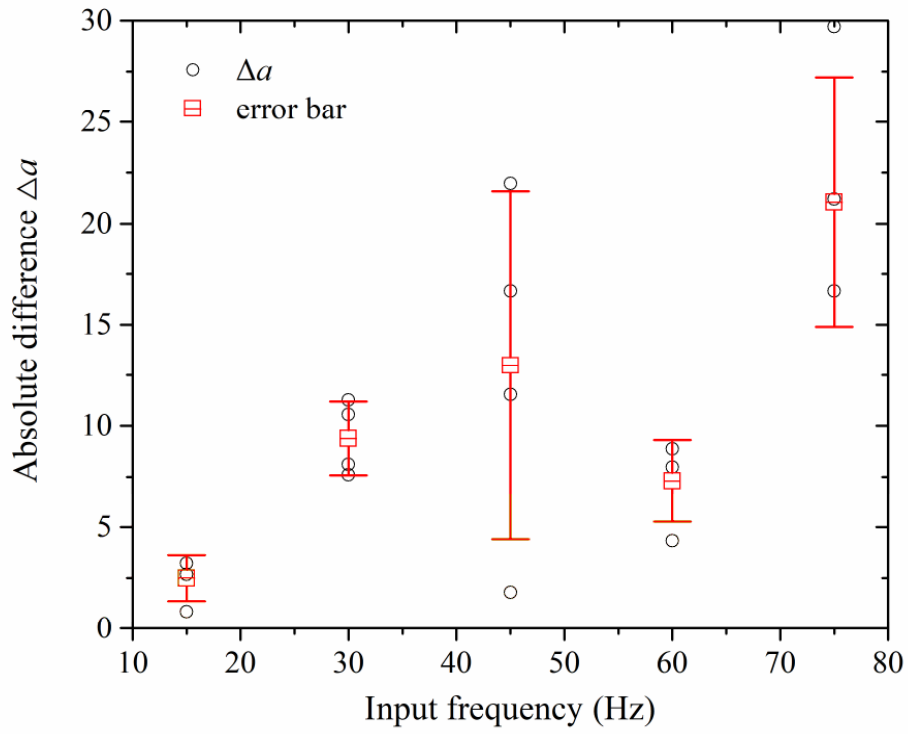


797

798 **Fig. 11** The AAF-Z change law of different sections (a) slope surface, (b) H1 and (c)

799 V1 under the excitation frequency 15 Hz

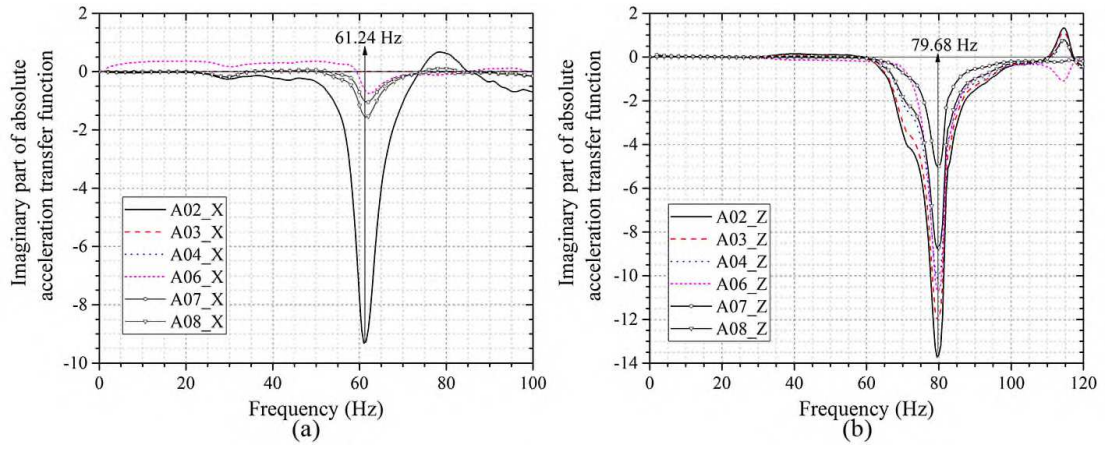
800



801

802 **Fig. 12** The absolute difference percentage (Δ) between accelerometer A19 and A18

803

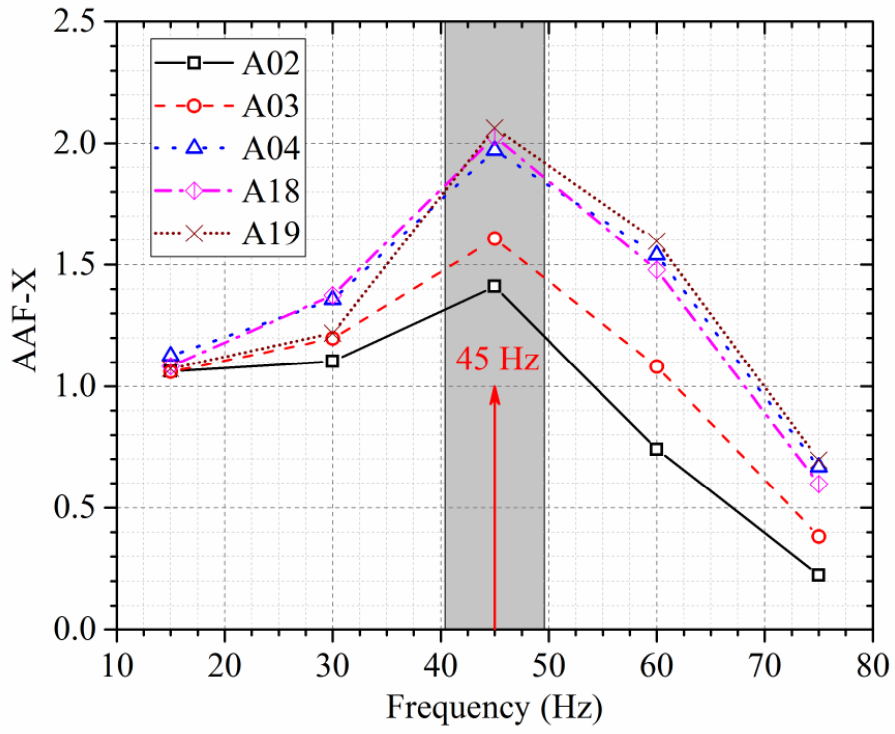


804

805 **Fig. 13** Transfer function curve obtained from first excitation of white noise: (a) X

806 direction and (b) Z direction

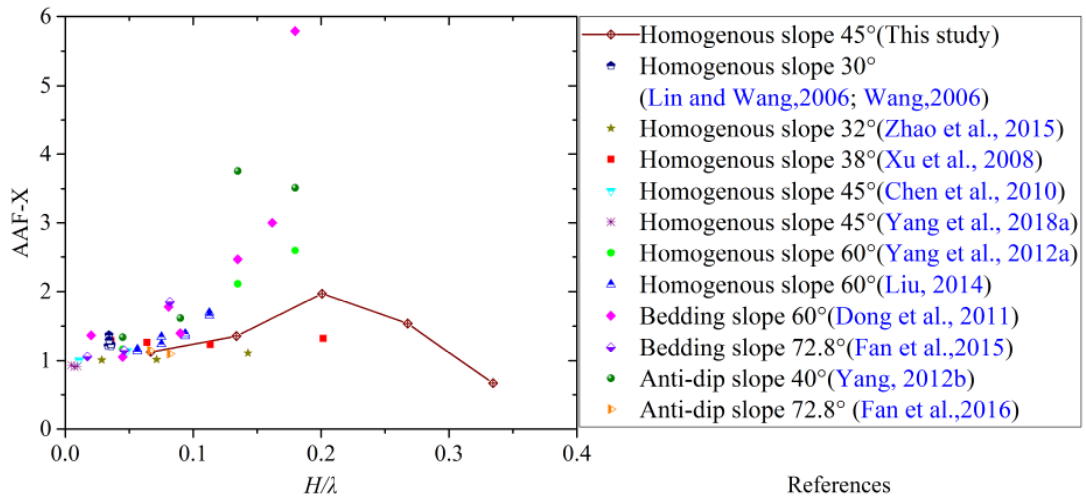
807



808

809 **Fig. 14** The AAF-X under different frequency excitations with amplitude 0.1g

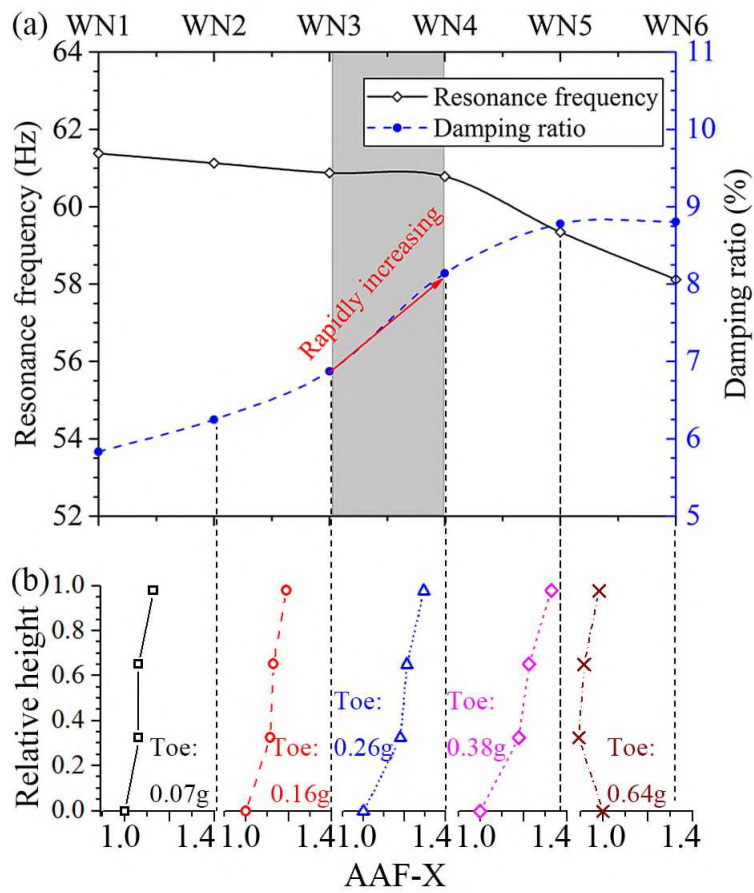
810



811

812 **Fig. 15** The AAF-X for different physical models with normalized parameter H/λ

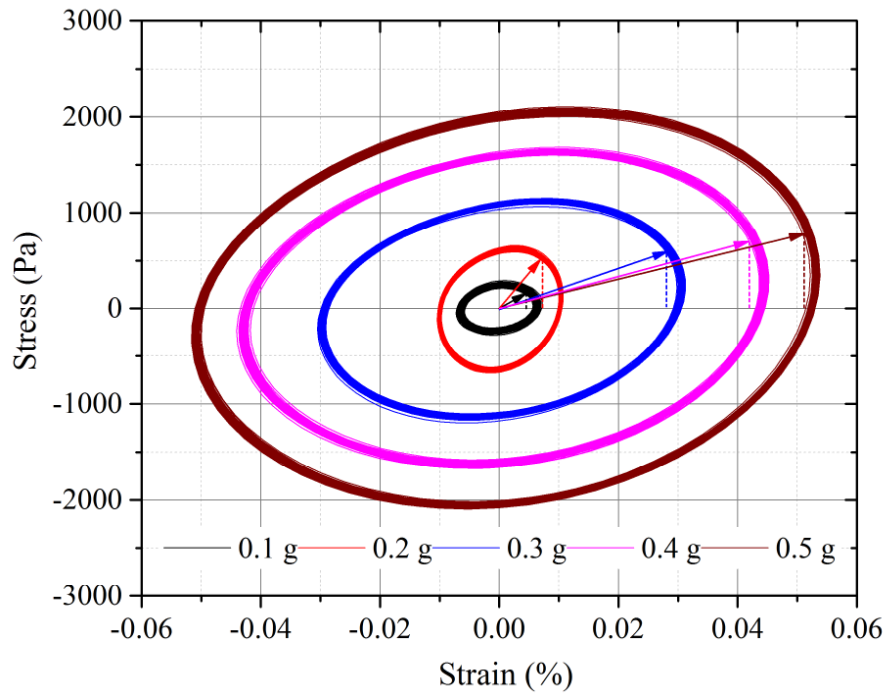
813



814

815 **Fig. 16** Resonance frequency and damping ratio under different WN stages

816

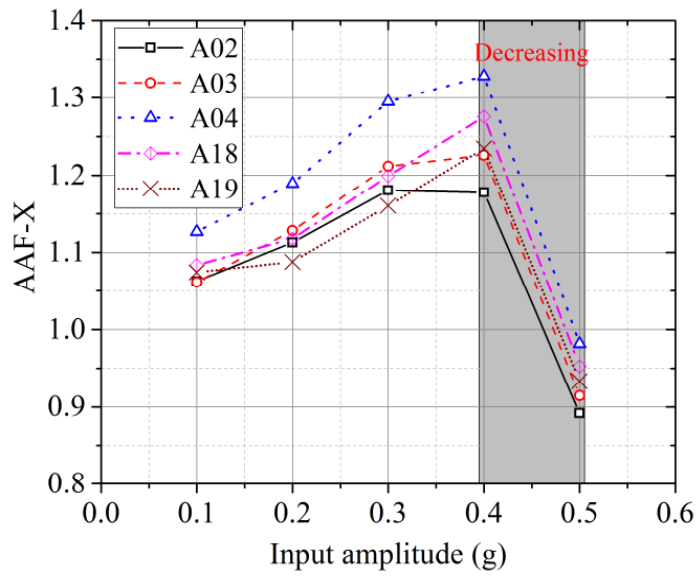


817

818 **Fig. 17** Shear stress–strain histories of the corresponding point between A04 and A15

819 under different amplitude excitation with frequency of 15 Hz

820



821

822 **Fig. 18.** The AAF-X of surface accelerometers under increase of amplitude excitation

823 with frequency of 15 Hz

824